





ARTICLE


<https://doi.org/10.1038/s41467-022-31212-8>

OPEN

Nuclear speed and cycle length co-vary with local density during syncytial blastoderm formation in a cricket

Seth Donoughe ^{1,6✉}, Jordan Hoffmann², Taro Nakamura ^{1,7}, Chris H. Rycroft ^{2,3✉} & Cassandra G. Extavour ^{1,4,5✉}

The blastoderm is a broadly conserved stage of early animal development, wherein cells form a layer at the embryo's periphery. The cellular behaviors underlying blastoderm formation are varied and poorly understood. In most insects, the pre-blastoderm embryo is a syncytium: nuclei divide and move throughout the shared cytoplasm, ultimately reaching the cortex. In *Drosophila melanogaster*, some early nuclear movements result from pulsed cytoplasmic flows that are coupled to synchronous divisions. Here, we show that the cricket *Gryllus bimaculatus* has a different solution to the problem of creating a blastoderm. We quantified nuclear dynamics during blastoderm formation in *G. bimaculatus* embryos, finding that: (1) cytoplasmic flows are unimportant for nuclear movement, and (2) division cycles, nuclear speeds, and the directions of nuclear movement are not synchronized, instead being heterogeneous in space and time. Moreover, nuclear divisions and movements co-vary with local nuclear density. We show that several previously proposed models for nuclear movements in *D. melanogaster* cannot explain the dynamics of *G. bimaculatus* nuclei. We introduce a geometric model based on asymmetric pulling forces on nuclei, which recapitulates the patterns of nuclear speeds and orientations of both unperturbed *G. bimaculatus* embryos, and of embryos physically manipulated to have atypical nuclear densities.

¹Department of Organismic and Evolutionary Biology, Harvard University, Cambridge, MA, USA. ²John A. Paulson School of Engineering and Applied Sciences, Harvard University, Cambridge, MA, USA. ³Computational Research Division, Lawrence Berkeley Laboratory, Berkeley, CA, USA. ⁴Department of Molecular and Cellular Biology, Harvard University, Cambridge, MA, USA. ⁵Howard Hughes Medical Institute, Chevy Chase, MD, USA. ⁶Present address: Department of Molecular Genetics and Cell Biology, University of Chicago, Chicago, IL, USA. ⁷Present address: Division of Evolutionary Development, National Institute for Basic Biology, Okazaki, Japan. ✉email: donoughe@uchicago.edu; chr@math.wisc.edu; extavour@oeb.harvard.edu

Proper positioning of nuclei is essential for cellular function^{1,2}. The task of correctly positioning nuclei is further specialized in syncytial cells—those with multiple nuclei sharing the same cytoplasm^{3,4}. Naturally occurring syncytia include animal muscle cells, heterokaryotic fungi, plant endosperm, and early cleavage stage arthropod embryos^{5–8}. Among arthropods, there have likely been multiple independent evolutionary origins of a syncytial phase of embryonic development⁸. Here, we focus on insects.

When an insect egg is fertilized, the oocyte and sperm pronuclei fuse, forming the zygotic nucleus within a single, large cell^{9,10}. In most insect taxa there follows a series of syncytial cleavages—nuclear divisions without cytokinesis^{9–11}. As the divisions proceed, nuclei move throughout the cytoplasm of the embryo. Although some nuclei remain submerged in the middle of the embryo, most of them travel into the periplasm, a region of cytoplasm at the periphery of the embryo^{9,10}. The nuclei in the periplasm comprise a syncytial blastoderm, a single layer of nuclei surrounding the cytoplasm in the interior^{9,10}.

Syncytial blastoderm formation has been studied most closely in the fruit fly *Drosophila melanogaster*^{12,13}. After fertilization, *D. melanogaster* undergoes 13 synchronous divisions¹². During cycles 4 through 6, nuclei spread out along the anterior-posterior (A-P) axis without entering the periplasm (a process referred to as “axial expansion”)^{13–16}. Nuclear movements along the A-P axis appear to be caused by the contraction of a subset of the cortex, which generates a cytoplasmic flow that carries nuclei towards the poles^{17,18}. It has also been suggested that local forces act on nuclei via their astral microtubules (MTs) pulling the nuclei toward the adjacent F-actin network¹⁹ and/or mutual repulsion among neighboring nuclei²⁰. Then, during cycles 7 through 9, the nuclei simultaneously move into the periplasm (leaving a small subset behind as “yolk nuclei,” also called “vitellophages”)^{9,20,21}. Finally, during cycles 10 through 13, the nuclei remain in the periplasm, arranged as a single layer^{15,21,22}. They increase in local nuclear density and assume an orderly geometric spacing^{23–28}.

Among insects with syncytially cleaving embryos, it appears to be universal that nuclei travel through the interior cytoplasm and into the periplasm^{9,10,29}, yet species differ dramatically with respect to the timing, speeds, and the paths that their nuclei traverse while getting there^{9,10,29}. This raises the question of how different insect species generate such embryological diversity. There is evidence from fixed preparations that some of the mechanisms described in *D. melanogaster*—namely cytoplasmic flows and MT-mediated pulling—might be operating in more distantly related insects^{30,31}. To assess such possibilities, quantitative, nucleus-level data on the dynamics of syncytial blastoderm formation are needed for species other than *D. melanogaster*. Therefore, we set out to investigate an informative comparator: the two-spotted field cricket *Gryllus bimaculatus* (order: Orthoptera).

G. bimaculatus is a powerful complement to *D. melanogaster* for the study of syncytial development. *G. bimaculatus* embryos are larger (approximately five-fold longer and three-fold wider)^{32,33} and their blastoderm formation occurs more slowly (14 hours at 28.5 °C versus 3 hours at 25 °C)^{22,34}. *G. bimaculatus* is hemimetabolous, and its embryonic development differs in many respects from that of *D. melanogaster* and other model holometabolous insect species³³. It likely retains many features of ancestral insect embryogenesis, unlike the relatively derived fruit fly model³³. Crucially, a transgenic line of *G. bimaculatus* expressing a constitutive ubiquitous Histone2B-Enhanced Green Fluorescent Protein (H2B-EGFP) fusion has been generated³⁴. The fusion protein presents a strong fluorescent contrast between syncytial nuclei and the surrounding cytoplasm during the entirety of pre-blastoderm development³⁴. This enabled us to

record, track, and analyze the movements of nuclei during syncytial development, starting from mitotic cycle ~2–4 and ending at the formation of the blastoderm.

We used multiview lightsheet and confocal microscopy to capture three-dimensional timelapse (3D + T) datasets and epifluorescence microscopy to capture two-dimensional timelapse (2D + T) datasets of syncytial development. We used a semi-automated approach to reconstruct nuclear tracks through space^{35,36}, and analyzed nuclear divisions, speeds, and movement orientations. We show that each of these nuclear behaviors covaries predictably with local nuclear density rather than with axial position, lineage, or developmental timing. We also show that the patterns of nuclear migration are more consistent with active movement through the cytoplasm, rather than with passive movement resulting from being carried along in a cytoplasmic flow. Based on our empirical description, and inspired by previously published work on active nuclear migration in other contexts^{19,37–40}, we built a simple computational model of nuclear movement based on asymmetric pulling forces and local interactions among nuclei. This model recapitulates the main features of *G. bimaculatus* nuclear divisions, speeds, and orientations during syncytial development. We tested the model by experimentally altering nuclear density, finding support for the hypothesis that a locally acting mechanism causes nuclear speed and density to co-vary predictably. Finally, we use this model to generate falsifiable hypotheses about blastoderm formation in other insect species.

Results

The *G. bimaculatus* syncytial blastoderm forms during approximately eight hours of development at 28.5 °C, followed by cellularization and coalescence of the embryonic rudiment^{33,34} (Fig. 1a). We recorded *G. bimaculatus* syncytial blastoderm formation *in toto* by using 3D + T lightsheet microscopy to image H2B-EGFP transgenic embryos. We tracked the movements and divisions of nuclei as they expanded throughout the embryo, which enabled us to reconstruct nuclear lineages (Fig. 1b) and quantify nuclear density, speed, and direction of movement. Similar to *D. melanogaster*^{13,15,16}, some nuclei appear to move in a highly directed manner toward the poles of the embryo (Fig. 1b, arrowhead). Unlike *D. melanogaster*, however, *G. bimaculatus* nuclei move into the periplasm asynchronously, with some reaching the periplasm 240 minutes after those that first reach it (Fig. 1b).

Nuclei are not predominantly moved by cytoplasmic flows. We wanted to determine whether nuclei are moved passively by being carried along in a cytoplasmic flow^{17,18}, or instead moved by a local active force^{19,20,31,38}. We generated a new stable transgenic line of *G. bimaculatus* that expressed myristoylated and palmitylated mTomato (mtdT) protein in the embryo. The mtdT protein is predominantly localized to the cytoplasm in the immediate vicinity of each syncytial nucleus (i.e. within the “energid”^{8,9}). It was excluded from putative yolk granules (Fig. 1c, white arrowheads; Supplementary Movie 1), but allowed us to see their outlines and follow their movements. We generated embryos that co-expressed mtdT and H2B-EGFP, which enabled us to image yolk granules and nuclear movements together (Fig. 1c; Supplementary Movie 1). We found that yolk granules and adjacent nuclei do not tend to move in the same direction together, even when they are quite close in space (e.g. within 40 μm, as shown in Fig. 1c and Supplementary Movie 1). This is inconsistent with a cytoplasmic flow that moves yolk granules and nuclei together. To further test the possibility of movement via cytoplasmic flows, we computed instantaneous pairwise

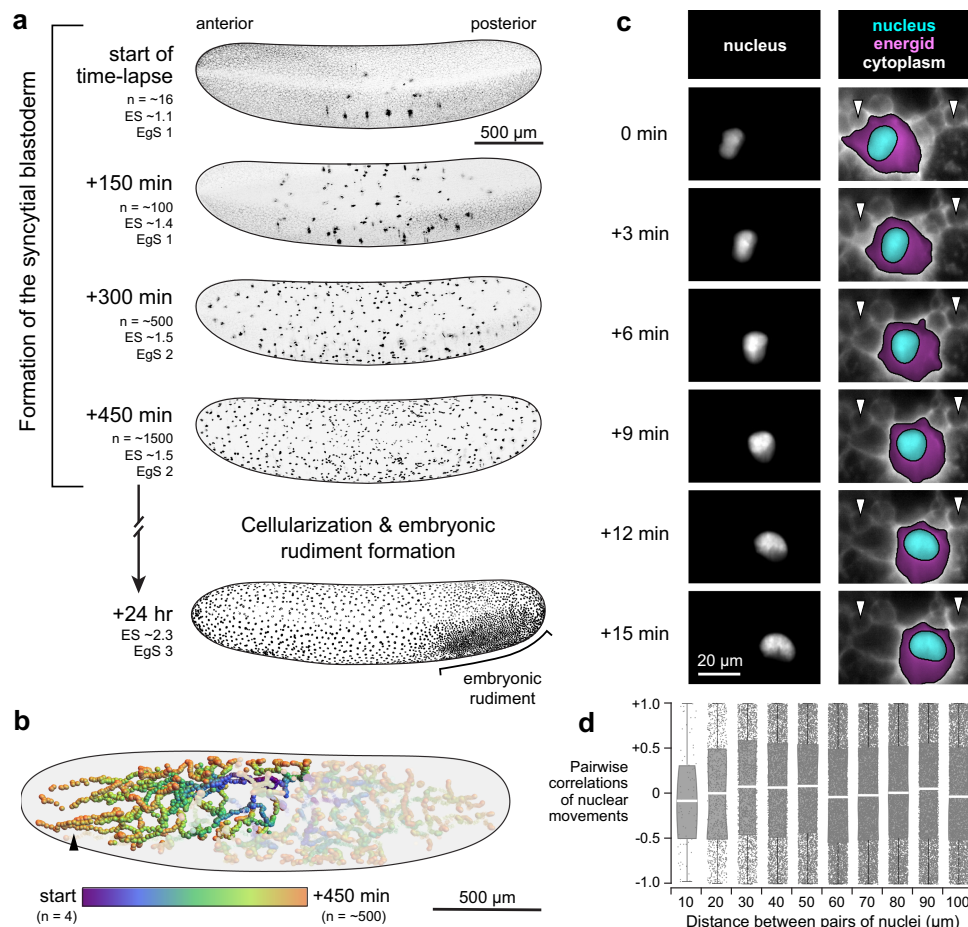


Fig. 1 Overview of *G. bimaculatus* blastoderm formation and evidence that nuclei move actively, rather than being moved passively by flowing cytoplasm. **a** Time points from the embryonic syncytial development of *G. bimaculatus*, displayed as z-projections of 3D stacks. Micrographs are from an H2B-EGFP transgenic *G. bimaculatus* embryo live-imaged using a lightsheet microscope over eight hours of development at 28.5 °C, capturing nuclear divisions and movements throughout the syncytial embryo. The nuclei (n) arrange into a single layer, after which cellularization occurs and the embryonic rudiment forms. Embryos are oriented laterally with ventral to the bottom and anterior to the left. Anterior is to the left in all subsequent figures. Embryonic stage (ES) and egg stage (EgS) are indicated for each time point³³. **b** Nuclei were tracked to produce a 3D + T dataset of nuclear lineages. All nuclear tracks are displayed for an example embryo, with the lineage descended from a single nucleus highlighted. Color scale represents time; n = number of nuclei. Black arrowhead highlights nuclei that move in a highly directed manner toward the anterior pole. **c** Example time points from a 3D + T dataset of a transgenic *G. bimaculatus* embryo with nuclei and cytoplasm fluorescently marked (further details in Methods). Left column shows the nucleus channel, and the right column shows the cytoplasm channel, with the energid cytoplasm highlighted in magenta and the nucleus highlighted in cyan. White arrowheads mark two putative yolk granules that remain in place as the nucleus moves past them. **d** Pairwise correlations between the instantaneous movement vectors of pairs of non-sister nuclei. White line indicates median, box indicates 25th–75th percentiles, whiskers show range. Source data are provided as a Source Data file.

correlations between the movement vectors of all pairs of nuclei. If nuclei were embedded in a cytoplasmic flow, we would expect nearby nuclei to move more similarly to one another than nuclei that were farther apart. This was not the case. Irrespective of pairwise distance, pairs of nuclei exhibit a random pattern of movement correlations (overall correlation of pairwise values with separation distance yields $R^2 = 0.032$; Fig. 1d; this calculation, and those presented in Fig. 2 and Fig. 3, was done on a dataset with 310,741 nucleus-timepoints). These observations suggest that *G. bimaculatus* syncytial nuclei are not predominantly moved by cytoplasmic flows.

Mitotic cycle duration is positively associated with local nuclear density. Previous work showed that syncytial nucleus divisions in *D. melanogaster* are synchronous, and that divisions are coupled to the nuclear movements that underlie blastoderm formation^{17,18}. We asked whether a similar mechanism operates

in *G. bimaculatus* embryos. For a coarse-grained measurement of proliferation, we calculated the percent change in the number of detectable nuclei over time (Fig. 2a). This metric displays a dynamic series of peaks and valleys, with each peak representing a pulse of divisions. These peaks occur initially at mean intervals of 49 minutes, and the time between peaks increases as development proceeds. This indicates that the cell cycle duration is approximately 49 minutes, which is a much greater time interval than the 8 to 9 minute cell cycle duration in a *D. melanogaster* embryo¹². The sharpness of the peaks attenuates over time, indicating a decrease in relative synchronicity (Fig. 2a). Next, we sought to determine whether the mitotic cycles are collectively going out of phase and/or the mitotic cycle lengths are themselves changing. We measured the cycle length of the nuclei, finding that it changes markedly over the course of blastoderm formation. An example lineage is shown in Fig. 2b. During four successive cycles, mean cycle length increases from 49 to 87 minutes (Fig. 2b). There is also considerable variation in cycle length

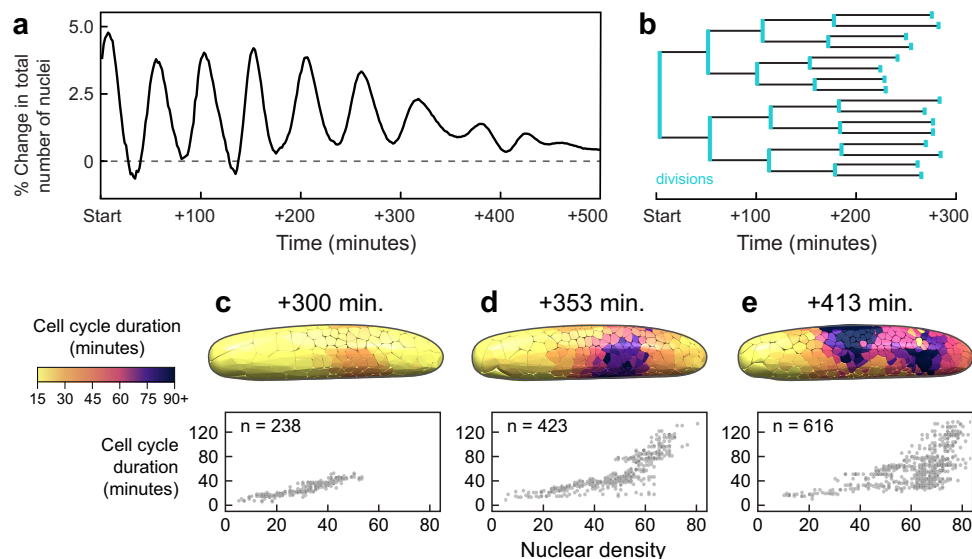


Fig. 2 Mitotic cycle duration covaries with nuclear density, explaining a marked decline in division synchronicity. **a** Percent change in the total number of observable nuclei over time. Divisions become increasingly asynchronous over the course of syncytial development. **b** Example lineage of dividing nuclei, starting with one of the nuclei at the four nucleus stage with divisions marked in turquoise. Over four division cycles, mean cycle duration increased from 49 to 87 minutes. **c–e** Cell cycle duration was positively associated with local density. Cell cycle duration was calculated in the vicinity of each nucleus by measuring the time elapsed until the number of nuclei within a 150 μm radius increased by 25%. Top row shows three example time points, with local cell cycle duration displayed as colored volumes, each of which contains a single nucleus. Bottom row shows scatterplots of the local cell cycle duration times and nuclear densities at each time point; n = number of nuclei. Source data are provided as a Source Data file.

among nuclei at the same cycle number (e.g. at cycle 4, SD of cycle length = 11 minutes; Fig. 2b). This is again in contrast to *D. melanogaster* embryos, in which cycle length increases over time, but all nuclei within a cycle have the same period^{21,41}. We hypothesized that in *G. bimaculatus*, variation in local nuclear density gives rise to the heterogeneity of cycle length. To test this, we computed the local nuclear density and proliferation time in the vicinity of each nucleus throughout blastoderm formation (three example time points are shown in Fig. 2c–e). Within each time point, we also took all possible nucleus pairs and computed the percentage of instances where the nucleus with the higher local density also had a longer proliferation time. These percentages are: $t = 300$ minutes: 91%, $t = 353$ minutes: 88%, $t = 413$ minutes: 75%. We concluded that there is a positive association between local nuclear density and mitotic cycle length across a range of local densities and throughout syncytial blastoderm formation.

Nuclear speed is biphasic and negatively associated with density. Given that a single variable—density—helped to explain both spatial and temporal variation in mitotic cycle length, we wondered whether the speeds of nuclear movements also followed a similar coherent pattern. We calculated instantaneous speed of all nuclei and then plotted those speeds over time (y) vs. position along the A-P axis (x) (Fig. 3a). Nuclear speed oscillates back and forth between “fast” and “slow” (> 4 to < 1 μm per minute, respectively). It appeared that in the central region of the embryo, farthest from the anterior and posterior poles, peak speeds decrease earlier, and the speed oscillations dissipate sooner than at either pole (Fig. 3a, middle of A-P axis, $t > 150$ minutes). To illustrate this further, we ordered the nuclei according to their position along the A-P axis and then partitioned them into three terciles, with equal numbers of nuclei in each one (labeled “anterior”, “middle”, and “posterior” terciles; Fig. 3b). When we plotted speed over time for the nuclei contained in each tercile, we observed that nuclear speed oscillates for all three terciles. In the middle tercile, however, where density is higher than in the

other terciles at every developmental time point examined, the oscillation is less pronounced and diminishes sooner, than in the anterior and posterior terciles (Fig. 3c). We also noticed that the speed oscillations are qualitatively similar to the oscillations of the percent change in total number of nuclei (compare Figs. 2a and 3c; $R^2 = 0.976$ for the correlation of the first six peaks from each dataset). Therefore, we hypothesized that each nucleus’s movements jointly depend on its local density and on the amount of time spent executing the cell cycle.

To test this, we computed time-since-last-division for each nucleus within the 200 minutes of development depicted in Fig. 3a. We divided the nuclei into three subsets according to their local nuclear density: “low,” “medium,” and “high” (< 11 , ≥ 11 and < 29 , ≥ 29 density units, defined here as the number of nuclei within a 150 μm radius). We plotted instantaneous nuclear speed for each density bin, with time re-zeroed to begin at the most recent division of each nucleus. This revealed density-associated speed oscillations for all nuclei, regardless of chronological age or spatial location within the egg (Fig. 3d). Nuclear speed alternated between relatively fast and slow phases, which we refer to as Phase A and Phase B, respectively. During Phase A, which is immediately after a division, each daughter nucleus moves relatively quickly (median Phase A speed: 2.3 μm per minute) for between 20 and 28 minutes. During Phase B, the nucleus remains largely stationary (median Phase B speed: 0.4 μm per minute) for between 10 and 20 minutes before again dividing and repeating this process (Fig. 3d). We plotted nuclear speed (y) vs. nuclear density (x) for Phase A and Phase B (Fig. 3e, f), and considering that both speed and density are by definition positive, in each case we fitted an exponential curve with the form $y = y_0 e^{-x/x_0}$. This yields a “density scale” (x_0) that captures how large of a change in density produces a given change in speed. The density scale of Phase A is 30.4 density units (90% CI: 28.8 to 32.1). For Phase B it is 120.4 density units (90% CI: 73.4 to 167.4). In sum, we found that Phase A nuclear movements have overall higher speeds that are strongly associated with density, while Phase B nuclear movements have lower speeds that are weakly

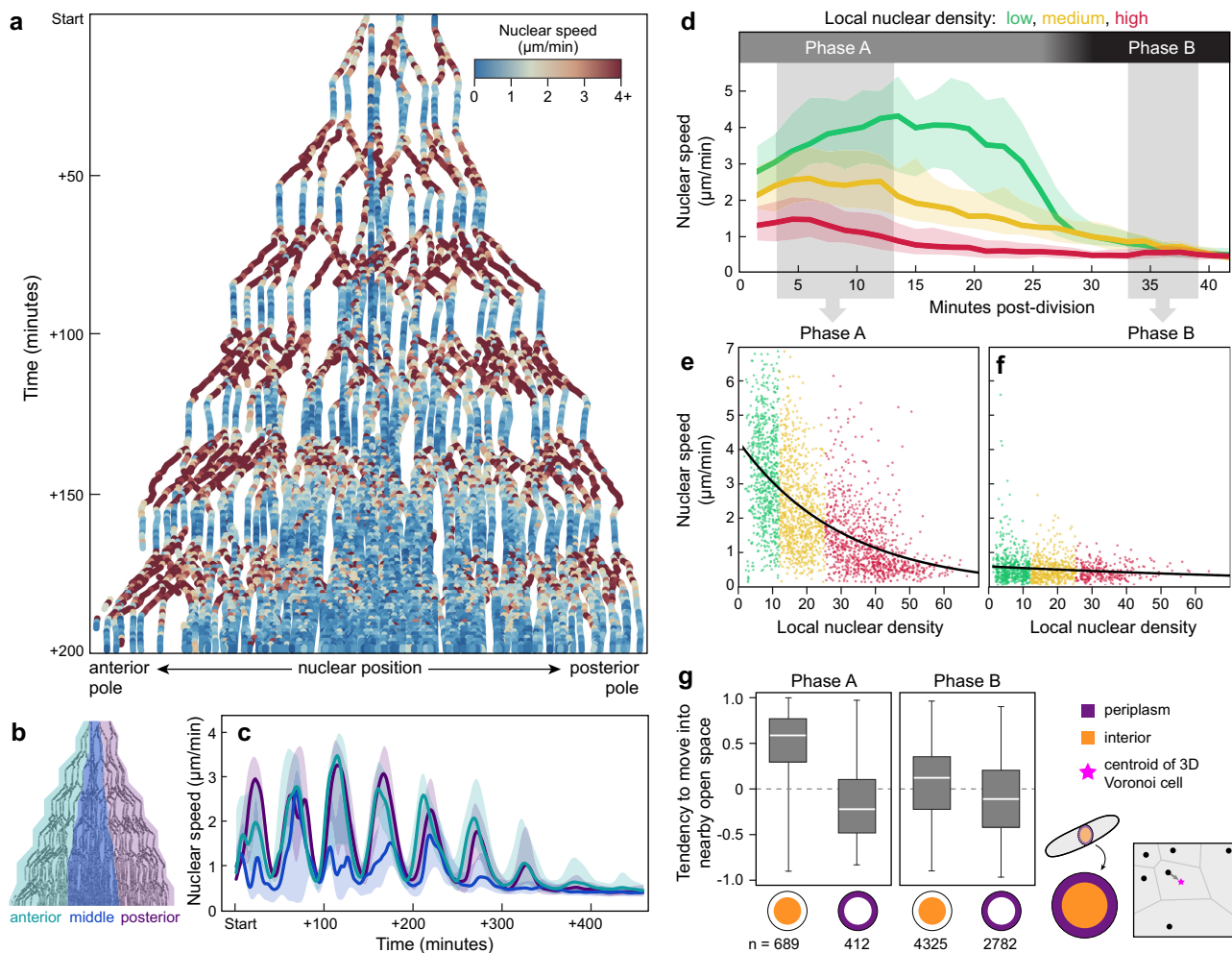


Fig. 3 After each division, nuclear speed covaries with local nuclear density, and nuclei move into nearby open space. **a** Nuclear positions along the anterior-posterior axis (x) over 200 minutes of syncytial development (y). Each dot represents a nucleus-timepoint, colored by its speed. The first zygotic division occurred ~60% from the anterior pole. Imaging began after the second division. **b** Schematic of nuclei, partitioned into anterior, middle, and posterior thirds (turquoise, dark blue, and purple, respectively). **c** Speed oscillations dissipate earliest in the middle third, where local nuclear density is highest. Center line represents median, shaded regions represent 25th–75th percentiles. **d–f** Nuclei from all time points and positions were grouped into bins, according to local density (number of nuclei within a 150-μm radius; “low”: < 11 nuclei, “medium”: ≥ 11 and < 29 nuclei, “high”: ≥ 29 nuclei). **d** Nuclear speed traces after each mitosis concluded. Nuclei move relatively quickly after a division and then slow down. We refer to these periods as “Phase A” and “Phase B”. Center line represents median, shaded regions represent 25th–75th percentiles. **e, f** Nuclear speed versus local density. Data are shown from two periods post-division: $t = 3$ to $t = 13.5$ min (**e**) and $t = 33$ min to $t = 39$ min (**f**). Black line is the best-fit curve of the form $y = y_0 e^{-x/x_0}$, yielding a density scale (x_0) of 30.4 density units for Phase A (90% CI: 28.8–32.1) and 120.4 density units for Phase B (90% CI: 73.4–167.4). **g** We calculated a nucleus’s tendency to move into nearby open space as its movement vector’s correlation with the vector from its current position to the centroid of its Voronoi cell (pink star). Nuclei were also subdivided into those in the “interior” of the embryo, or in the periplasm (defined here as within 75 μm of the eggshell). The distribution of single time-step nuclear movements (n) is shown for each bin. Phase A nuclei in the interior tend to move into nearby open space, but not when they are in the periplasm (left). Phase B nuclei tend not to do so regardless of where they are (right). White line represents median, boxes represent 25th–75th percentiles, whiskers show range. Source data are provided as a Source Data file.

associated with local density. We concluded that nuclear speeds covaried with local nuclear density and time in the cell cycle.

In the cytoplasm, nuclei tend to move into nearby unoccupied space. Nuclear speed alone cannot achieve axial expansion: nuclei also need to move in appropriate directions to ensure even distribution of nuclei in the blastoderm. The directionality cannot be uniform for all nuclei, however, otherwise all nuclei would end up crowded together in a single region of the embryo. To investigate what might predict directionality, we began by observing the global features of nuclear paths during syncytial blastoderm formation. Once syncytial nuclei reach the periplasm, they remain there until cellularization occurs^{13,34} (Fig. 1a, b), suggesting that

G. bimaculatus nuclei, like *D. melanogaster* nuclei, ultimately become anchored in the periplasm^{15,42–45}. Compared to the synchronously emerging nuclei of *D. melanogaster*¹⁵, however, *G. bimaculatus* nuclei move along trajectories that are varied, with some reaching the periplasm as many as 240 minutes later than others (Fig. 1a, b). We hypothesized that as *G. bimaculatus* nuclei move through the cytoplasm, they preferentially move into nearby unoccupied space, which might explain the diversity of traveled paths.

To test this hypothesis, we binned nuclei into those that are in the periplasm and those that are not (Fig. 3g, schematized in orange and purple at right). Then, for the nuclei in each subset we calculated a “space-seeking score”, defined as the correlation of a nucleus’s instantaneous movement vector with the vector that is

oriented toward the most open space relative to the positions of its neighbors in 3D space (schematized in Fig. 3g, bottom right; see details of this calculation in the Supplemental Information). We found that when they are not in the periplasm, Phase A nuclei tend to move into nearby open space (median space-seeking score = 0.61; Fig. 3g), whereas Phase B nuclei do not (median space-seeking score = 0.12; Fig. 3g). Once nuclei reach the periplasm, however, they do not tend to move into open space during either Phase A or Phase B (median space-seeking score = -0.21 and -0.10, respectively; Fig. 3g). Consequently, they remain in the periplasm once they arrive there, forming the blastoderm, rather than moving back into the central yolk mass. We concluded that except for when they are in the periplasm, Phase A nuclei move preferentially into nearby unoccupied space.

A simulation framework of cricket syncytial development. We asked whether the nuclear movements during *G. bimaculatus* blastoderm formation could be explained by models that had been previously proposed for nuclear movement in other contexts. We considered three such candidate models of nuclear movement: (1) Cytoplasmic flows that move nuclei^{17,18}; (2) Mutual, repulsive, active forces among nuclei^{20,46}; (3) Local, asymmetric, active pulling forces on each nucleus^{19,37–40}. This modeling effort was an attempt to assess the relative plausibility of broad bins of explanations for the forces that generate nuclear movements, which could serve as a guide to future molecular-scale empirical work.

These modes of movement are not necessarily mutually exclusive¹³, yet for the sake of computational tractability, we assessed each of them in turn. The results presented in Fig. 1c and d contradicted the cytoplasmic flow model (1), so we did not consider it further. Similarly, we found that the empirical data contradicted the mutual repulsion model (2). Specifically, in models with mutual repulsion of nuclei, the magnitude of repulsion is highest when nuclei are closest to one another, and it attenuates with increased distance^{25,39}. If a model assumes that a nucleus's speed is directly related to the magnitude of the net force it experiences, a nucleus should move at its lowest speed when it is at the lowest density, i.e. when it is maximally distant from other nuclei. This is the opposite of what we observed in *G. bimaculatus* (Fig. 3e). In *D. melanogaster*, however, recent work on the spacing among nuclei at the syncytial blastoderm stage led to models of mutual nuclear repulsion with symmetric, mutual pushing forces^{25,47}. To further evaluate the possibility of model (2), mutual nuclear repulsion in forming the *G. bimaculatus* blastoderm, we selected the model of Dutta and colleagues²⁵, adapted it to 3D, and implemented it in a simulation framework of preblastoderm syncytial nuclear movements in *G. bimaculatus*. We found that it did not produce a negative relationship between nuclear density and speed at any of the parameter settings we assessed (see Supplementary Note 5.1). We also implemented a new, asymmetric pushing model, which likewise generated a pattern of nucleus movements that was dramatically different from those of real embryos (see Supplementary Note 5.2). Therefore, we did not consider pushing models further, and instead developed (3), a simplified geometric model of a local, asymmetric, active pulling force on each nucleus. Below, we summarize the key features and assumptions of the model.

Our model was inspired by research on nuclear movements in the red bread mold *Neurospora crassa*, the filamentous fungus *Aspergillus nidulans*, the nematode worm *Caenorhabditis elegans*, and *D. melanogaster*, which presented evidence for pulling forces on astral MTs and the microtubule-organizing center (MTOC) associated with each nucleus^{19,37,38,40,48,49}. In the present study,

without specific empirical data on the cytoskeletal structures in the *G. bimaculatus* embryo, we abstracted the MT aster and MTOC contributions to the model as a “cloud” and “cloud origin”, respectively (schematized in Fig. 4a). We posited that, as in other systems^{37,48,50,51}, cytoplasmic dyneins or functionally analogous molecules exert pulling forces on the astral MTs. We considered the dyneins to be uniformly distributed in the cytoplasm, and implemented their pulling forces as tugs on each voxel on the surface of each cloud. We divided each tug by a factor of R^2 where R represented the distance from the voxel to its cloud origin. Scaling the relative strengths of the forces in this manner is analogous to a set of rods emanating from a point on the nucleus, normalized such that the total pull on a rod was proportional to its length, similar to previous work on *C. elegans* nucleus movement⁵². The sum of all the forces on a cloud origin causes nuclei to move through space and/or rotate. Larger and more asymmetric clouds therefore apply a relatively larger net pulling force (schematized in Fig. 4a). The clouds regrow after each division, but their growth is occluded by one another and by the internal surface of the simulated eggshell (Fig. 4b). If simulated nuclei proliferate in a limited volume, local density increases, which means that over time, clouds grow smaller (Fig. 4c, d). Each nucleus cycles from a Phase A (faster) state to a Phase B (slower) state, then it divides and returns to Phase A. During Phase A, the nucleus's cloud grows to its maximum size (unless spatially constrained) and exerts pulling forces on the nucleus. During Phase B, the cloud is absent.

Here, we briefly describe the full set of inputs to the model; for further details of its computational implementation see Section 4 of the SI. The model was run in a bounded volume that had the same morphology as a real embryo (Supplementary Note 4.1.1). All mitotic division orientations were random (Supplementary Note 4.1.2). Each nucleus was assigned a cycle length based on its local nuclear density. These cycle lengths were drawn from a distribution that was fitted to the empirical density-cycle length relationship (Supplementary Note 4.1.3). The maximum radius of each pulling cloud was set to 150 μm ; this is the same size as the local neighborhood that we used to detect the empirical associations between nuclear density and cycle length (Fig. 2c–f), as well as between nuclear density and Phase A speed (Fig. 3e). To assign a magnitude to the pulling forces exerted by the clouds, we calibrated it by fitting a constant factor so that the maximum empirical speed of simulated nuclei matched that of the nuclei in a real embryo (Supplementary Note 4.1.4). We also found that in real embryos, nuclei traveled varied paths with most of them ultimately reaching the periplasm and staying there. It is unknown what causes this periphery-bias in *G. bimaculatus*. In the model, we represented this bias as a small, constant component of each nucleus's movement vector at each time step, tuning its magnitude to match the rate at which real nuclei moved towards the periplasm in empirical data (Supplementary Note 4.1.5).

The model did not include terms for fluid flows, nor maternally provided signals in the yolk, nor any direct mechanical interaction between the force-generating regions around nuclei, each of which is a relevant parameter regulating axial expansion or patterning in the *D. melanogaster* embryonic syncytium^{18,27,53}. As in previous work modeling nuclear movements in a syncytial blastoderm²⁵, we worked in the overdamped limit where viscosity is so large that force was proportional to velocity (see Supplementary Note 4.1 for details). In summary: the model was designed to implement only *local* and *density-associated* effects on nuclear behavior. None of the fitted parameters change as a function of spatial position within the embryo, nor do they change as a function of developmental time. We used this model to determine whether this set of local interactions was sufficient

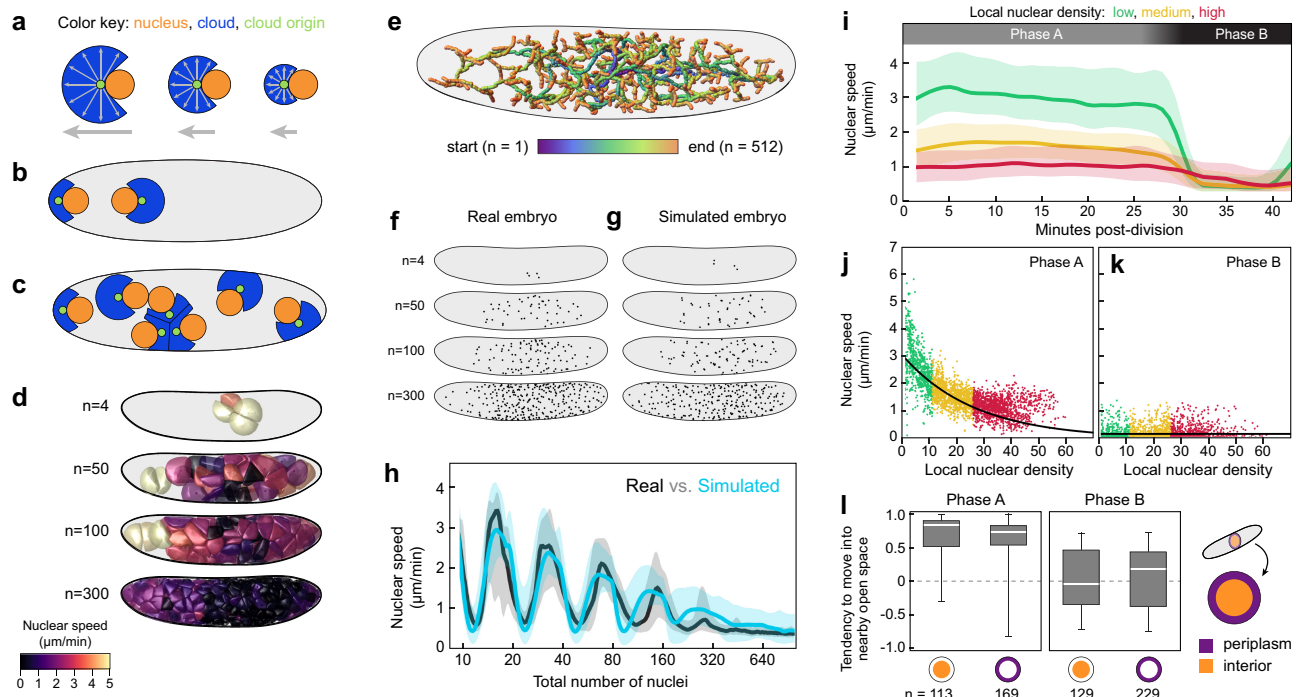


Fig. 4 A simple model based on local pulling clouds recapitulates many features of *G. bimaculatus* syncytial development. **a–c** Method for simulating syncytial development, schematized in 2D (not to scale). **a** Each nucleus (orange) moves due to a pull from a “cloud” (blue) that grows from a “cloud origin” (green) on the nucleus. Each voxel within a cloud pulls on the nucleus via its origin point (small arrows). The nucleus occludes symmetrical growth of the cloud; thus, the cloud is asymmetric and the net pull on the nucleus is determined by the cloud’s size and shape (large arrows). **b** Before a division, two cloud origins are assigned random positions opposite one another on the nuclear surface. Then the nucleus divides. Each daughter nucleus inherits a cloud origin, which grows a new cloud. The eggshell occludes the growth of clouds. **c** Nuclei proliferate and spread. Growing clouds occlude one another; therefore, as local nuclear density increases, clouds are unable to grow as large. Consequently, nuclear speeds are lower in regions with higher nuclear density. The model also includes a general bias in movement toward the periplasm (not depicted). **d** Simulated clouds, colored by their nuclear speeds. **e** 3D paths of simulated nuclei. **f, g** z-projections of nuclear positions in example real (**f**) and simulated (**g**) embryos, stage-matched by total number of nuclei (n). **h** Whole-embryo nuclear speed (y) vs. total nuclear number (x , log scale) from a simulated (turquoise) and real (black) embryo (line represents median, shaded region represents 25th–75th percentiles). **i–l** Simulated nuclear speeds and directions co-vary with density and cycle phase, similar to empirical patterns (see Fig. 3d–g). **i** Simulated nuclear speed traces after division. **j, k** Nuclear speed vs. local density. Best-fit density scale (x_0) was 26.8 density units for Phase A (90% CI: 24.2–29.3) and 12,108 density units for Phase B (90% CI: 11,124–13,092). **l** Simulated single time-step nuclear movements (n). Simulated Phase A nuclei in the interior and periplasm tend to move into nearby open space (left). Simulated Phase B nuclei tend not to do so regardless of where they are (right). White line represents median, boxes represent 25th–75th percentiles, whiskers show range. Source data are provided as a Source Data file.

to recapitulate the spatiotemporal distributions of nuclei in wild-type and experimentally altered embryos.

Simulation results. First, we wanted to determine whether our implementation of local pulling clouds could generate a density-speed relationship and space-seeking behavior like those of real embryos. As in Fig. 3e and f, we fitted a curve to the speed vs. nuclear density relationship, which yielded density scales for Phases A (faster) and B (slower) of 26.8 density units (90% CI: 24.2 to 29.3) and 12,108 density units (90% CI: 11,124 to 13,092), respectively. Nuclei in the simulated embryo, like those in real embryos, exhibit a negative relationship between density and speed in Phase A (Fig. 4j). In Phase B, with no pulling clouds, nuclear speed does not vary with density at all (Fig. 4k). We also assessed the tendency of nuclei to move into unoccupied space. As in real embryos, simulated nuclei that are not in the periplasm tend to move into unoccupied space during Phase A (median space-seeking score = 0.86) but not during Phase B (median space-seeking score = -0.04; Fig. 4l). However, once simulated nuclei are in the periplasm, unlike in real embryos, simulated nuclei still tend to move into nearby open space during Phase A (median space-seeking score = 0.75; compare Fig. 4k to Fig. 3f). In *D. melanogaster* there is a cytoskeletal mechanism that holds

nuclei in place once they reach the periplasm^{15,42–45}. We suggest that there is likely a similar mechanism at work in *G. bimaculatus* that has not been included in our model.

Next, we wanted to determine whether the spatial and temporal patterns of *G. bimaculatus* nuclear movements and positions could be recapitulated solely by the local interactions included in our pulling model. Indeed, we found that although the model did not include any whole-embryo global spatial information, it nevertheless recapitulated the overall spatial distribution of nuclei along the anterior-posterior axis throughout the course of syncytial development (Fig. 4f, g). Similarly, we found that the geometric arrangement of nuclei of the simulated embryo matched that of the real embryo (Fig. 4f, g). In the pulling simulation, the existence of speed oscillations, and an overall tendency for nuclei in higher densities to have longer cell cycles, both result directly from the way the model was fitted to the empirical data. Thus, neither of those features should be viewed as confirmatory results from the modeling. However, although nothing in the model prescribed the decay in speed peaks over developmental time, nuclei in simulated embryos recapitulated the empirically observed time course of speed peak decay (Fig. 4h). This means that the density-dependent mitotic cycle length relationship, calibrated from empirical nucleus-level data,

was sufficient to reproduce the spatiotemporal nuclear proliferation patterns across entire the embryo. In light of the simulation results, we concluded that a local, asymmetric, active pulling force on each nucleus is consistent with most of the observed nuclear behaviors in *G. bimaculatus*.

Constricting embryos. Based on the empirical data and simulation results, we hypothesized that the negative relationship between nuclear density and speed emerges only as a consequence of local spatial constraints generated by an asymmetric pulling mechanism. With the descriptive data and simulations alone, however, we could not rule out the possibility that the observed changes in nuclear speed were caused by a spatially localized or temporally varying signal in the cytoplasm. Therefore, to test our hypothesis and assess the alternatives, we experimentally altered the density of nuclei, accomplished by physically manipulating the geometry of embryos. We designed and built a device to constrict an embryo from the outside by wrapping a human hair around it and incrementally increasing the tension on the hair. Specifically, we constricted *G. bimaculatus* embryos width-wise at the beginning of syncytial development, and then mounted them in a glass bottom dish for epifluorescence microscopy (Fig. 5a; see Supplementary Note 6 for detailed methods and Supplementary Software 1 for the design file of the device's components). With this mode of microscopy, we collected 2D + T datasets, imaging nuclei through approximately one-third of the *z* depth of the embryo. This imaging modality necessitated 2D measures of speed and density. Those measures and the total nucleus counts were not comparable on an absolute scale to the equivalent values in the 3D + T datasets. Thus, for these analyses, we compared between and within embryos that were all imaged using epifluorescence microscopy. The first zygotic nuclear division typically occurs approximately 60% from the anterior pole along the length of the embryo. We constricted embryos at a position 25% to 35% from the anterior pole (Fig. 5a). By pinching a region down to approximately one-third of the radius of the embryo, we generated two pseudo-compartments in the embryo, each of which was smaller than an unconstricted embryo (Fig. 5b). In both pseudo-compartments of the constricted embryos, the patterns of nuclear density over time and space differed markedly from those of unmanipulated embryos, which enabled us to decouple nuclear speed and density from any as-yet undetected spatially localized cytoplasmic determinants.

First, we compared nuclear behavior between posteriors of constricted embryos to unconstricted embryos. In effect, this allowed us to control for A-P position and developmental time while changing nuclear density. To compare the data from multiple embryos on a single plot, we stage-matched datasets ($n = 3$ embryos per treatment) by the total number of nuclei in each embryo as a proxy for developmental time. As nuclei divide and move within a constricted posterior volume, the total space available to them is reduced compared to an unmanipulated embryo, which causes them to experience higher densities earlier in development than they would otherwise (Fig. 5c). For instance, when there were 200 total nuclei, median density was 20.1 density units in constricted embryos (25th percentile = 18.1, 75th percentile = 22.2) and 15.2 density units in unconstricted embryos (25th percentile = 11.0, 75th percentile = 19.5). The higher density nuclei in constricted embryos moved more slowly than those in stage-matched unmanipulated embryos where the density was lower (Fig. 5d). At 200 total nuclei, median speed was 0.68 μm per minute in constricted embryos (25th percentile = 0.57, 75th percentile = 0.73) and 0.93 μm per minute in unconstricted embryos (25th percentile = 0.85, 75th percentile

= 1.06). Last, we computed all instantaneous nuclear speeds and densities in each constricted posterior and unconstricted dataset, finding that nuclei follow the same density-speed relationship in constricted and unconstricted embryos (Fig. 5e). These results are consistent with a mechanism in which local geometric constraints produce a negative relationship between nuclear speed and density, rather than nuclear speed responding to anteroposterior position or developmental time.

The constricted embryos provided the opportunity to analyze nuclei not only under ectopically high local nuclear densities, but also under ectopically low densities. The latter becomes possible when, in constricted embryos, some nuclei traverse the constricted region and populate the formerly unoccupied pseudo-compartment (Fig. 5a). These nuclei move into a low density region from a comparatively high density region, creating an abrupt change in local density for a subset of nuclei. With this experiment, we altered the developmental time-course of densities that the nuclei experienced. We quantified the nuclear speeds under these conditions, and plotted nuclear speed vs. time for the posterior (ectopically high density) and anterior (ectopically low density) subsets of nuclei (Fig. 5f). We observed that posterior nuclei undergo speed oscillations and overall decreasing speeds, similar to nuclei in unperturbed embryos. We also observed that 50 to 80 minutes after the start of each dataset, nuclei emerge from the constriction (indicated by dotted lines; Fig. 5f), whereupon they speed up as they populate the unoccupied space, slowing down again once local nuclear density increases, ultimately coming to match the speeds of the nuclei in the posterior (compare magenta to orange speed traces; Fig. 5f). We interpreted these results as further evidence of a local mechanism that causes nuclear speed to co-vary negatively with density, which functions independently of developmental time and spatial location.

Simulating blastoderm formation for embryos with other shapes. We wanted to know whether our model, parameterized and validated on unmanipulated *G. bimaculatus*, could successfully predict nuclear behaviors in a constricted embryo. We used the same simulation procedure described above, changing only the geometry of the embryo to a constricted shape (Fig. 5g, h). The simulated pulling clouds completely fill the posterior compartment before any nuclei emerge through the constriction (Fig. 5g). This results in a distribution of nuclei over time in the simulations that is qualitatively similar to that of the real constricted embryos (Fig. 5h; compare to 5a). As in the real embryos, the simulated nuclei also exhibit speed oscillations that get slower and with smaller amplitude over time in each pseudo-compartment, but that pattern is offset in time and space for nuclei in the anterior, which abruptly speed up once they pass through the constriction (Fig. 5h). We concluded that simulations broadly recapitulated the experimental results from an atypical embryo geometry, and interpreted this as further support for a model of local, asymmetric, active pulling forces on *G. bimaculatus* syncytial nuclei.

With the aim of uncovering mechanistic principles that might extend beyond this specific case, we asked whether this predictive model of nuclear behavior, derived from observations on *G. bimaculatus*, could be generalized to describe axial expansion in the syncytial embryos of other insects. As a first step in this direction, we asked how well the parameterized model would perform at simulating blastoderm formation in insect species that are either more closely or distantly related to *G. bimaculatus*. The locust *Schistocerca gregaria* is an orthopteran insect, like *G. bimaculatus*, but lays eggs that are 2.5 times longer and 1.5 times wider than *G. bimaculatus* eggs^{33,54}. The first nuclear division in

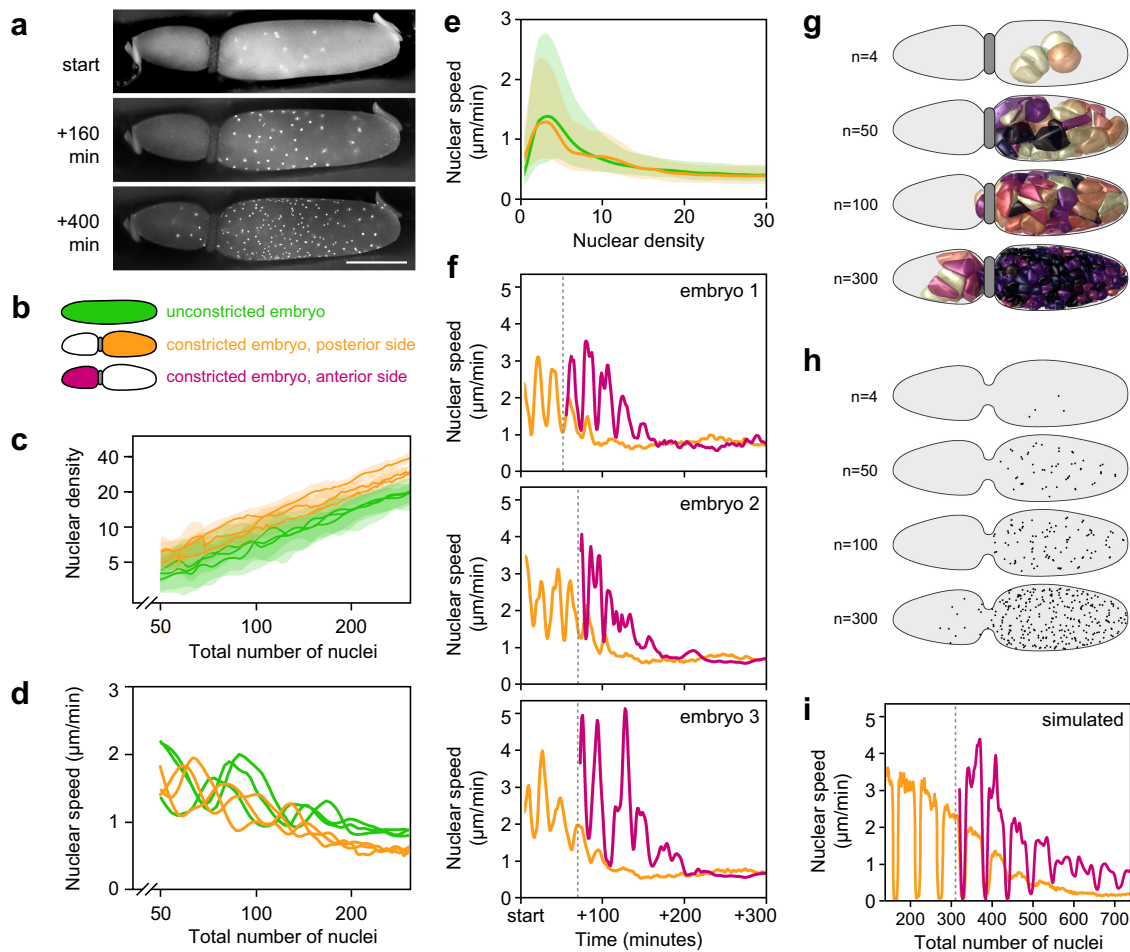


Fig. 5 Embryo constrictions demonstrate that nuclear density, rather than spatially or temporally localized signals, determines nuclear speed. **a** Three time points of an embryo, constricted with a human hair (see Supplemental Note 6), imaged with epifluorescence microscopy. Scale bar represents 500 μm . **b** Color key and schematic for subsets of nuclei represented in this figure. **c** Nuclear density (y , log scale) plotted against total number of nuclei (x , log scale) for unconstricted embryos (green; $n=3$) and the posterior side of constricted embryos (orange; $n=3$). Line represents median, shaded regions represent 25th–75th percentiles of each embryo's data. Constrictions caused higher nuclear densities for a given number of total nuclei. **d** Median nuclear speed (y) vs. total number of nuclei (x , log scale) for the same datasets as in **c**. As the posterior sides of constricted embryos fill with nuclei, local densities increase and nuclear speeds decrease, as compared to unconstricted embryos. **e** Nuclear speed (y) vs. density (x) for all movements in the datasets shown in **c** and **d**. Embryonic constrictions do not change the relationship between speed and density. Center line represents median, shaded regions represent 25th–75th percentiles. **f** Median nuclear speed (y) over time (x) for three example constricted embryos. Posterior and anterior nuclei are shown in orange and magenta, respectively. Vertical dotted line indicates the timepoint when nuclei first emerge from the constriction into the anterior side. When the nuclei emerge, they speed up as they populate the unoccupied compartment of the embryo, slowing again once local nuclear density increases. **g–i** Our model of pulling clouds (see Fig. 4) qualitatively recapitulated empirical nuclear behaviors in a simulated constricted embryo. **g** 3D renderings of pulling clouds from four selected time points of a simulation of syncytial blastoderm formation in a constricted embryo. Each cloud is colored according to the speed of its nucleus, following the colormap in Fig. 4d. **h** z -projections of nuclear positions in a simulated constricted embryo. **i** Median nuclear speed (y) vs. total number of nuclei (x) for a simulated constricted embryo, plotted as in **f**. Source data are provided as a Source Data file.

S. gregaria also occurs closer to the posterior pole than that of *G. bimaculatus*^{54–56}. We deployed the computational model described earlier in the text, leaving all parameters the same except for two changes: (1) the morphology of the embryo was set to be an ellipsoid with the volume and approximate shape of the *S. gregaria* embryo;⁵⁴ (2) the position of the first division was set to 85% from the anterior pole along the length of the embryo, similar to that of *S. gregaria*⁵⁴. Based on comparisons to previous work that used fixed embryo preparations, and acknowledging differences in imaging modality, we observed some similarities and some differences between the features of nuclear positioning in the simulated embryo and in real locust embryos⁵⁴ (Fig. 6a, b). One similarity was that nuclei reach the posterior pole of the embryo while the anterior two-thirds of the embryo are still

devoid of nuclei. Another is that nuclei form a gradient in their spacing, with the largest internuclear distances at the anterior of the expanding front of nuclei (compare Fig. 6a and b). A detectable difference, however, is that in the real locust embryo, the region with the highest density of nuclei is at the very posterior tip of the embryo. In the simulated embryo, the region with the highest nuclear density remained instead at the position where the first zygotic division occurred. In fact, this was a general outcome in all of our simulations under this model, regardless of embryo shape or size. This could mean that for species whose region of highest nuclear density is far from the position of the earliest division, our model may not effectively describe nuclear behavior in those species without an additional parameter to create directed nuclear migration. We hypothesize

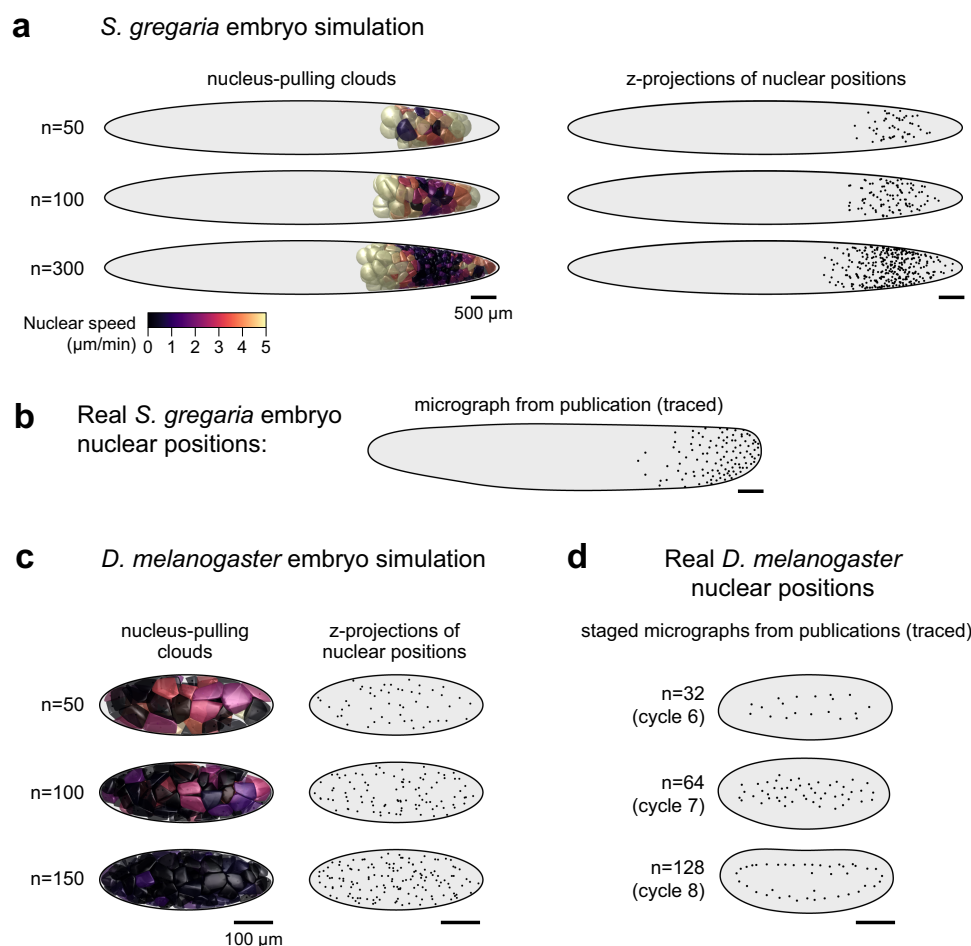


Fig. 6 The parameterized model of local pulling clouds qualitatively recapitulates blastoderm formation of another orthopteran, but not *D.*

melanogaster. **a** Selected time points of simulated blastoderm formation in an ellipsoid with the length and width of the locust *Schistocerca gregaria* embryo. The location of the first division was set to 85% from the anterior pole along the length of the embryo, as in *S. gregaria*⁵⁴. Left column: 3D renderings of pulling clouds, colored by simulated nuclear speed. Right column: z-projections of simulated nuclear positions. **b** Tracing of a fixed preparation of a *S. gregaria* at 16 hours after egg laying (AEL) at 29 °C and imaged in a manner that captured a subset of the z depth of the embryo⁵⁴. **c** Selected time points of simulated blastoderm formation in an ellipsoid with the length and width of the *D. melanogaster* embryo. Left column: 3D renderings of pulling clouds, colored by instantaneous speed. Right column: z-projections of simulated nuclear positions. **d** Tracings of published micrographs of *D. melanogaster* embryos from cycle 6, 7, and 8 from Baker and colleagues²⁰ (cycles 6 and 8) and Deneke and colleagues¹⁸ (cycle 7). In both sources, a subset of the z depth of the embryo was imaged^{18,20}. For each cycle, the total number of nuclei is shown in parentheses¹⁵.

that a mechanism of local, asymmetric, active pulling forces also operates in the *S. gregaria* preblastoderm embryo, with a possible bias in movement toward the posterior of the embryo.

By contrast, our parameterized model, run with the *D. melanogaster* embryo morphology and first division location, produces arrangements of nuclei that differ qualitatively from those of real *D. melanogaster* embryos. The simulated nuclei spread throughout the volume of the embryo by moving in all directions, with some moving into the periplasm before the rest (Fig. 6c). In real embryos, nuclei spread out predominantly along the A-P axis without moving into the periplasm, then form an ordered shell-like arrangement^{18,20} (Fig. 6d), followed by simultaneous movements into the periplasm^{20,21} (not depicted in the schematic). We interpret this result as evidence against the hypothesis that there is a shared cellular mechanism that scales with embryo size to generate preblastoderm nuclear behavior across insect taxa¹⁹. This result is also consistent with recent work on *D. melanogaster*, which demonstrated that cytoplasmic flows generate some of the preblastoderm nuclear movements¹⁸. In the future it will be fruitful to use experimentally validated

computational models to develop hypotheses for nuclear dynamics in other poorly studied systems.

Discussion

Our computational model was inspired by empirical descriptions of astral MTs and nuclear movements in other contexts^{1,19,37,40}. Given the model's effectiveness in capturing *G. bimaculatus* nuclear dynamics, we speculate that cytoplasmic dyneins interacting with astral MTs may indeed be the most likely molecular cause of the asymmetric pulling forces on *G. bimaculatus* syncytial nuclei. There is evidence that such a mechanism may also be present in *D. melanogaster* embryos but obscured by the comparatively dramatic effect of cytoplasmic flows¹⁸; nuclei in non-flowing cytoplasmic extracts of preblastoderm *D. melanogaster* embryos move apart from one another in a MT- and centrosome-dependent manner that appears to be consistent with a pulling force on asters¹⁹. If MT-mediated forces are responsible for syncytial nuclear movements, it will be important to know whether the astral MTs are interdigitating and mechanically

interacting^{20,27}. Such interactions are absent from our model, but if they were shown to be relevant for *G. bimaculatus*, future modeling work would need to represent the astral MTs in a finer-grained manner than the simple clouds that we described here. Alternatively, asymmetric active forces in *G. bimaculatus* could be generated by a molecular mechanism that does not involve dynein and astral MTs³⁹. One possibility is that dynamic remodeling of the actin cytoskeleton in the immediate neighborhood of a nucleus could generate nucleus movements by local, asymmetric fluidization¹⁶. Another is that asymmetric contractile interactions within an actomyosin network at the periphery of each energid could pull an energid—and the nucleus embedded within it—through the rest of the cytoplasm. It is also possible that MTs and actomyosin contractility jointly contribute to nuclear movements^{13,16,57}. For instance, one way that MTs and F-actin can affect nuclear movement was recently shown in *D. melanogaster* blastoderm stage embryos: during a wave of divisions, the ensemble of mitotic spindles drives anisotropic nuclear movement of nuclei, which then return to their original positions in an F-actin-dependent manner²⁶.

The results of the present study enable us to make inferences about cytoplasmic signals that may regulate the cell cycle behaviors of nuclei during *G. bimaculatus* syncytial development. Similar to *D. melanogaster*¹⁹, *G. bimaculatus* nuclei speed up after each division and then slow down, which suggests that the mechanism driving nuclear movement is coupled to the cell cycle. In *D. melanogaster*, changes in the localization and activity of cytoplasmic Cdk1 and CycB over the course of the cell cycle affect MT and actomyosin dynamics^{17,18,58}. We hypothesize that the nucleus-moving mechanism in *G. bimaculatus* is affected in a similar, cell cycle-coupled manner. Unlike *D. melanogaster*^{19,21,41,59}, however, *G. bimaculatus* cycle duration appears to be locally responsive to nuclear density, rather than coordinated throughout the entire embryo. It has been shown that experimentally increased levels of CycB protein reduce the duration of interphase in *D. melanogaster*⁴¹, and that CycB is degraded at a subcellular spatial scale⁶⁰. Therefore, one possibility is that in *G. bimaculatus*, regions with relatively high nuclear density locally reduce the levels of CycB (or a protein with an analogous function), which causes the duration of interphase to increase accordingly. If true, diffusion would not be predicted to generate uniform cytoplasmic protein levels on relevant time scales in the much larger *G. bimaculatus* embryos. In general, such a mechanism would be consistent with the comparatively heterogeneous cell cycle durations in *G. bimaculatus*. It is also not known how the local environment around each nucleus may change to cause them to stop moving during the latter portion of each cell cycle. During the “slow” phase (Phase B), the MT asters might be absent altogether, or present as a balanced pair on each nucleus¹⁹. Further descriptive work characterizing MT dynamics in real embryos will be needed to determine which of these best explains the biphasic speed pattern in *G. bimaculatus* nuclei during axial expansion.

Our results have implications for the mechanisms governing subsequent *G. bimaculatus* development. Researchers have begun to describe some of the earliest patterning events in *G. bimaculatus*, including aspects of the establishment of the A-P axis, the dorsal-ventral axis, and the bipartition of the blastodermal cells into embryonic and extraembryonic tissues^{34,61–63}. The present study demonstrates that the early *G. bimaculatus* embryo does not have stereotypic divisions nor movements, but instead each nucleus’s behavior is determined by the geometry of its neighbors. Collectively, these stochastic interactions, constrained by local rules, generate an emergent uniform spacing of blastodermal nuclei across the embryo. Accordingly, we hypothesize that any maternally provided axial patterning information, if present, is likely to be “stored” in the central cytoplasmic mass or in the

periplasm. We also hypothesize that any such putative localized signals will not have a detectable effect on syncytial nuclear behavior. By extension, we predict that the subdivision of the blastoderm into the embryonic anlage and extraembryonic tissues⁶³ is not determined during the preblastoderm stage, and that the two populations of cells only become separate lineages after a blastoderm has formed.

The computational model we present for blastoderm formation enables us to make predictions about early embryogenesis in other insect species. Insect eggs have a wide range of shapes and sizes^{64,65}, and the egg determines the shape and size of the syncytial embryo^{9,10}. In our simulations, embryo morphology—as well as the location of the initial zygotic division—plays a major role in determining patterns of nuclear movement over the course of blastoderm formation. If an asymmetric pulling mechanism drives syncytial nuclear movements in other insect species, we predict that patterns of syncytial nuclear behavior will tend to co-vary predictably with egg morphology. For instance, in an embryo with a higher aspect ratio^{64,65} we would predict a front of low-density nuclei moving at relatively high speeds into unoccupied regions of the embryo, trailed by nuclei arranged in a density gradient (and exhibiting concomitant speeds and cell cycle durations). In a spherical embryo (i.e. an aspect ratio of 1) with a centrally located first zygotic nucleus, we would expect comparatively uniform movements and densities over time and space. In smaller embryos, nuclei would reach an equilibrium spacing more quickly than in larger embryos. These predictions could be tested in a straightforward manner by comparing timed and fixed embryo preparations from insect species that are closely related, yet have embryos of different sizes and/or shapes.

We suggest that elements of the empirical and modeling approaches in the current study could also be fruitfully applied to better understand nuclear behaviors in other multinucleate cell types. In mammalian muscle cells, there are numerous types of nuclear movement, with distinct cellular mechanisms implicated in each one^{4,66,67}. Likewise, in filamentous fungi, nuclei are moved by several mechanisms, with important roles for cytoplasmic dynein and astral MTs^{3,68}. Arbuscular mycorrhizal fungi have multinucleate spores with hundreds of nuclei, organized in a shared volume, but the cellular mechanisms underlying this arrangement are not known^{69,70}. It will be illuminating to discover the ways in which MT- and F-actin-based molecular mechanisms are deployed in different distantly related species to generate forces on nuclei, moving them into the proper arrangement at the right time and place. Comparing such mechanisms across taxa will provide insight into how the conserved eukaryotic cellular machinery shapes developmental evolution.

Methods

Transgenesis and animal culture. *G. bimaculatus* cultures were maintained at 28.5 °C in plastic cages, fed dry cat food (Purina Kitten Chow), and supplied with wet cotton in plastic tubes for hydration³³. We used an established nucleus-marked transgenic line of *G. bimaculatus*³⁴, in which the endogenous *actin* promoter drives expression of the *G. bimaculatus* Histone 2B (H2B) protein fused to Enhanced Green Fluorescent Protein (EGFP) (this transgenic line is abbreviated hereafter as Act-H2B-EGFP). To label cytoplasm and nuclei together, we generated a new transgenic insertion of a myristoylated and palmitoylated tandem dimer Tomato fluorescent protein (hereafter: mtdT) expressed under the control of the *G. bimaculatus actin* promoter. The mtdT-3xHA sequence was obtained from pUASTattB-mtdT-3XHA⁷¹ (Addgene Plasmid #24355), and cloned into the pXL[Gbact-GFP-pA] vector³⁴ in place of GFP, to create pXL[Gbact-mtdT-3xHA-pA]. We used this plasmid to generate a stable transgenic line of *G. bimaculatus* by co-injecting it with a plasmid containing the piggyBac transposase coding sequence, and then screening embryos in the next generation for stable transgenic expression³⁴. We crossed the Act-mtdT and Act-H2B-EGFP lines to obtain mature F1 females with both transgenes, assessed by using a fluorescence dissection microscope to check for red and green fluorescent protein expression in late embryogenesis. These F1 females with both

transgenes matured to adulthood, and then were crossed to wild-type males. F2 eggs were collected for live imaging. Thus, when imaging the mtdT and H2B-EGFP transgenic proteins in the same embryo, both were maternally provided to the embryos.

Collecting and culturing embryos. To collect embryos for live imaging, females were allowed to lay eggs in damp sand for two hours at a time, and then the eggs were separated from the sand with a sieve³³. Embryos were examined on a fluorescence dissection microscope within five hours of collection. If there were between 2 and 8 nuclei visible, then embryos were mounted for microscopy as described below under *Microscopy*. After imaging, embryos were placed in a 10 mm diameter plastic petri dish (VWR 25384-342), the bottom of which had been covered with Kimwipes (VWR 21905-026) moistened with distilled water. We incubated the dish at 28.5 °C so that embryos could continue to develop. We checked embryos daily and removed any dead ones. Only datasets from embryos that hatched within 16 days of being laid were used for analysis.

Microscopy. For 3D + T lightsheet imaging, we mounted embryos individually in a column of 1% (w/v) low-melt agarose (Bio-Rad 1613112) in distilled water. Suspended in the mounting agarose were 1 µm diameter red fluorescent polystyrene beads (ThermoFisher F8821) at 0.015% of the stock concentration. Lightsheet imaging was conducted with a Zeiss Z.1 Lightsheet microscope controlled by Zen Black software (Zeiss, 2014-2018), with the agarose column immersed in a bath of distilled water, temperature controlled at 28.5 °C. Embryos were imaged one at a time, positioned with the A-P axis oriented vertically. For each time point, z-stacks were captured at 72 ° or 90 ° increments, rotationally distributed about the long axis of the egg. Data were simultaneously captured with 488 nm and 568 nm lasers at a time interval of 90 seconds, with 100 to 200 optical sections per z-stack. Among lightsheet datasets, z-step size ranged from 4 to 10 µm, depending on the overall size of the field of view needed to capture the embryo. For 3D + T imaging of cytoplasm and nuclei together, we individually mounted embryos in a glass-bottom dish (MatTek P06G-1.5-20-F) in a 20 µL puddle of molten 0.5% (w/v) low-melt agarose in distilled water. Then we covered the immobilized embryos in distilled water and imaged them on a Zeiss LSM 880 confocal microscope at 28.5 °C. For 2D + T imaging of whole embryos, they were mounted in agarose microwells⁷² and imaged using epifluorescence on a Zeiss Cell Discoverer microscope with a 5x objective, controlled with Zen Blue (Zeiss, 2015-2018). Epifluorescence datasets were captured as a z-stack at each time point. Embryo constrictions were conducted with a custom device that is described in Supplementary Note 6. A design file of the device's components is included as Supplementary Software 1.

Image processing and segmentation. Lightsheet datasets were processed using the Multiview Reconstruction plug-in for Fiji (version 2.0.0-rc-30 to 2.1.0/1.5.3)^{73,74}. In epifluorescence datasets, z-slices were combined using the Extended Depth of Focus function (Contrast mode) in Zen Blue (Zeiss, 2015-2018). Confocal datasets were processed in Fiji to generate maximum intensity projections. Nucleus tracks were generated with Ilastik³⁶ and manually corrected with Fiji plug-in MaMuT (2018 version)³⁵. Additional image processing details are included in the Supplementary Note 1.

Measuring and simulating quantitative features of nuclear behavior. Data analysis and simulations of nuclear movements were performed using custom scripts written in Mathematica (Wolfram, versions 11 and 12) and Python 3. Python code used functions from the following packages: numpy (version 1.18.1), scipy (version 1.4.1), scikit-fmm (version 2019.1.30). We calculated nuclear speed, local nuclear density, rate of change in number of nuclei, and movement toward nearby unoccupied space. See Supplementary Note 2 for the specifics of these calculations and Supplementary Notes 4 and 5 for a detailed description of nuclear movement simulations.

Figure preparation. Micrographs for presentation were processed in Fiji⁷⁵. Figures were generated with Mathematica and assembled with Illustrator (Adobe).

Reporting summary. Further information on research design is available in the Nature Research Reporting Summary linked to this article.

Data availability

The data that support this study are available from the corresponding authors upon reasonable request. For all data that were generated in this study, quantitatively analyzed, and then presented as graphs, see the included source data. Additional tracked nucleus data are available at the GitHub repository for this project: https://github.com/hoffmannjordan/gryllus_nuclear_movements⁷⁶. Animals from the *G. bimaculatus* culture are available for sharing from the corresponding authors upon request, provided that the requestor obtains the necessary permits for the transfer and continued maintenance of the culture (the specific permits vary by jurisdiction). The plasmid for

generating the Act-mtdT transgenic line described in the present study will likewise be available from the corresponding authors upon reasonable request. Source data are provided with this paper.

Code availability

The aforementioned GitHub repository includes the code used to simulate nuclear movements during blastoderm formation and the code used to convert the tracking output from Ilastik into an XML file that was parsable by MaMuT.

Received: 26 April 2021; Accepted: 9 June 2022;

Published online: 06 July 2022

References

- Reinsch, S. & Gönczy, P. Mechanisms of nuclear positioning. *J. Cell Sci.* **111**, 2283–2295 (1998).
- Morris, N. R. Nuclear migration: from fungi to the Mammalian brain. *J. Cell Biol.* **148**, 5 (2000).
- Fischer, R. Nuclear movement in filamentous fungi. *FEMS Microbiol. Rev.* **23**, 39–68 (1999).
- Roman, W. & Gomes, E. R. Nuclear positioning in skeletal muscle. *Semin. Cell Dev. Biol.* **82**, 51–56 (2018).
- Kim, J. H., Jin, P., Duan, R. & Chen, E. H. Mechanisms of myoblast fusion during muscle development. *Curr. Opin. Genet. Dev.* **32**, 162–170 (2015).
- Strom, N. B. & Bushley, K. E. Two genomes are better than one: history, genetics, and biotechnological applications of fungal heterokaryons. *Fungal Biol. Biotechnol.* **3**, 4 (2016).
- Plachno, B. J. & Świątek, P. Syncytia in plants: cell fusion in endosperm—placental syncytium formation in *Utricularia* (Lentibulariaceae). *Protoplasma* **248**, 425–435 (2011).
- Scholtz, G. & Wolff, C. Arthropod embryology: cleavage and germ band development. In *Arthropod Biology and Evolution* (eds. Minelli, A., Boxshall, G. & Fusco, G.) 63–89 (Springer Berlin Heidelberg, 2013). https://doi.org/10.1007/978-3-662-45798-6_4.
- Anderson, D. T. Development of holometabolous insects. In *Developmental Systems: Insects*. (ed. Counce, S. J.) Volume I, 165–242 (1972).
- Anderson, D. T. Development of hemimetabolous insects. In *Developmental Systems: Insects*. (ed. Counce, S. J.) Volume I, 95–163 (1972).
- Johannsen, O. A. & Butt, F. H. *Embryology of insects and myriapods*. (McGraw-Hill Book Company, Inc., 1941).
- Foe, V. E., Odell, G. M. & Edgar, B. Mitosis and morphogenesis in the *Drosophila* embryo: point and counterpoint. 149–300 (Cold Spring Harbor Laboratory Press, 1993).
- Lv, Z., de-Carvalho, J., Telley, I. A. & Großhans, J. Cytoskeletal mechanics and dynamics in the *Drosophila* syncytial embryo. *J. Cell Sci.* **134**, jcs246496 (2021).
- Sonnenblick, B. The early embryogenesis of *Drosophila melanogaster*. In *The Biology of Drosophila*. (ed. Demerec, M.) 62–167 (Wiley, New York, 1950).
- Zalokar, M. & Erk, I. Division and migration of nuclei during early embryogenesis of *Drosophila melanogaster*. *J. Microsc. Biol. Cell* **25**, 97–106 (1976).
- von Dassow, G. & Schubiger, G. How an actin network might cause fountain streaming and nuclear migration in the syncytial *Drosophila* embryo [published erratum appears in *J Cell Biol* 1995 Sep;130(5):1231-4]. *J. Cell Biol.* **127**, 1637–1653 (1994).
- Royou, A., Sullivan, W. & Karsenti, R. Cortical recruitment of nonmuscle myosin II in early syncytial *Drosophila* embryos: its role in nuclear axial expansion and its regulation by Cdc2 activity. *J. Cell Biol.* **158**, 127–137 (2002).
- Deneke, V. E. et al. Self-organized nuclear positioning synchronizes the cell cycle in *Drosophila* embryos. *Cell* **177**, 925–941.e17 (2019).
- Telley, I. A., Gáspár, I., Ephrussi, A. & Surrey, T. Aster migration determines the length scale of nuclear separation in the *Drosophila* syncytial embryo. *J. Cell Biol.* **197**, 887–895 (2012).
- Baker, J., Theurkauf, W. E. & Schubiger, G. Dynamic changes in microtubule configuration correlate with nuclear migration in the preblastoderm *Drosophila* embryo. *J. Cell Biol.* **122**, 113–121 (1993).
- Foe, V. E. & Alberts, B. M. Studies of nuclear and cytoplasmic behaviour during the five mitotic cycles that precede gastrulation in *Drosophila* embryogenesis. *J. Cell Sci.* **61**, 31–70 (1983).
- Foe, V. E., Field, C. M. & Odell, G. M. Microtubules and mitotic cycle phase modulate spatiotemporal distributions of F-actin and myosin II in *Drosophila* syncytial blastoderm embryos. *Development* **127**, 1767–1787 (2000).
- Kanesaki, T., Edwards, C. M., Schwarz, U. S. & Grosshans, J. Dynamic ordering of nuclei in syncytial embryos: a quantitative analysis of the role of cytoskeletal networks. *Integr. Biol.* **3**, 1112–1119 (2011).

24. Kaiser, F. et al. Mechanical model of nuclei ordering in *Drosophila* embryos reveals dilution of stochastic forces. *Biophys. J.* **114**, 1730–1740 (2018).
25. Dutta, S., Djabrayan, N. J.-V., Torquato, S., Shvartsman, S. Y. & Krajnc, M. Self-similar dynamics of nuclear packing in the early *Drosophila* embryo. *Biophys. J.* **117**, 743–750 (2019).
26. Lv, Z. et al. The emergent Yo-yo movement of nuclei driven by cytoskeletal remodeling in pseudo-synchronous mitotic cycles. *Curr. Biol.* **30**, 2564–2573.e5 (2020).
27. Deshpande, O., de-Carvalho, J., Vieira, D. V. & Telley, I. A. Astral microtubule cross-linking safeguards uniform nuclear distribution in the *Drosophila* syncytium. *J. Cell Biol.* **221**, e202007209 (2022).
28. de-Carvalho, J., Tlili, S., Hufnagel, L., Saunders, T. E. & Telley, I. A. Aster repulsion drives local ordering in an active system. <https://doi.org/10.1101/2020.06.04.133579> (2020).
29. Kessel, E. L. The embryology of fleas. *Smithson. Misc. Collect.* **98**, 1–78 (1939).
30. Eastham, L. A contribution to the embryology of *Pieris rapae*. *J. Cell Sci.* **2**, 353–394 (1927).
31. Wolf, R. Migration and division of cleavage nuclei in the gall midge, *Wachtliella persicariae* II. Origin and ultrastructure of the migration cytaster. *Wilhelm. Roux' Arch. Für. Entwicklungsmechanik Org.* **188**, 65–73 (1980).
32. Markow, T. A., Beall, S. & Matzkin, L. M. Egg size, embryonic development time and ovoviviparity in *Drosophila* species. *J. Evol. Biol.* **22**, 430–434 (2009).
33. Donoughe, S. & Extavour, C. G. Embryonic development of the cricket *Gryllus bimaculatus*. *Dev. Biol.* **411**, 140–156 (2016).
34. Nakamura, T. et al. Imaging of transgenic cricket embryos reveals cell movements consistent with a syncytial patterning mechanism. *Curr. Biol.* **20**, 1641–1647 (2010).
35. Wolff, C. et al. Multi-view light-sheet imaging and tracking with the MaMuT software reveals the cell lineage of a direct developing arthropod limb. *eLife* **7**, e34410 (2018).
36. Berg, S. et al. ilastik: interactive machine learning for (bio)image analysis. *Nat. Methods* **16**, 1226–1232 (2019).
37. Gönczy, P., Pichler, S., Kirkham, M. & Hyman, A. A. Cytoplasmic dynein is required for distinct aspects of MtoC positioning, including centrosome separation, in the one cell stage *Caenorhabditis elegans* embryo. *J. Cell Biol.* **147**, 135–150 (1999).
38. Kimura, K. & Kimura, A. Intracellular organelles mediate cytoplasmic pulling force for centrosome centration in the *Caenorhabditis elegans* early embryo. *Proc. Natl Acad. Sci. USA* **108**, 137–142 (2011).
39. Gundersen, G. G. & Worman, H. J. Nuclear positioning. *Cell* **152**, 1376–1389 (2013).
40. De Simone, A., Spahr, A., Busso, C. & Gönczy, P. Uncovering the balance of forces driving microtubule aster migration in *C. elegans* zygotes. *Nat. Commun.* **9**, 938 (2018).
41. Ji, J.-Y., Squirrell, J. M. & Schubiger, G. Both cyclin B levels and DNA-replication checkpoint control the early embryonic mitoses in *Drosophila*. *Development* **131**, 401–411 (2004).
42. Buttrick, G. J. et al. Akt regulates centrosome migration and spindle orientation in the early *Drosophila melanogaster* embryo. *J. Cell Biol.* **180**, 537–548 (2008).
43. Edgar, B. A., Odell, G. M. & Schubiger, G. Cytoarchitecture and the patterning of fushi tarazu expression in the *Drosophila* blastoderm. *Genes Dev.* **1**, 1226–1237 (1987).
44. Sullivan, W., Fogarty, P. & Theurkauf, W. Mutations affecting the cytoskeletal organization of syncytial *Drosophila* embryos. *Development* **118**, 1245–1254 (1993).
45. Riggs, B. et al. Actin cytoskeleton remodeling during early *Drosophila* furrow formation requires recycling endosomal components Nuclear-fallout and Rab11. *J. Cell Biol.* **163**, 143–154 (2003).
46. Anderson, C. A. et al. Nuclear repulsion enables division autonomy in a single cytoplasm. *Curr. Biol.* **23**, 1999–2010 (2013).
47. Koke, C., Kanesaki, T., Grosshans, J., Schwarz, U. S. & Dunlop, C. M. A computational model of nuclear self-organisation in syncytial embryos. *J. Theor. Biol.* **359**, 92–100 (2014).
48. Plamann, M., Minke, P. F., Tinsley, J. H. & Bruno, K. S. Cytoplasmic dynein and actin-related protein Arp1 are required for normal nuclear distribution in filamentous fungi. *J. Cell Biol.* **127**, 139–149 (1994).
49. Suelmann, R., Sievers, N. & Fischer, R. Nuclear traffic in fungal hyphae: in vivo study of nuclear migration and positioning in *Aspergillus nidulans*. *Mol. Microbiol.* **25**, 757–769 (1997).
50. Inoue, S., Turgeon, B., Yoder, O. & Aist, J. Role of fungal dynein in hyphal growth, microtubule organization, spindle pole body motility and nuclear migration. *J. Cell Sci.* **111**, 1555–1566 (1998).
51. Burakov, A., Nadezhkina, E., Slepchenko, B. & Rodionov, V. Centrosome positioning in interphase cells. *J. Cell Biol.* **162**, 963–969 (2003).
52. Kimura, A. & Onami, S. Computer simulations and image processing reveal length-dependent pulling force as the primary mechanism for *C. elegans* male pronuclear migration. *Dev. Cell* **8**, 765–775 (2005).
53. St Johnston, D. & Nüsslein-Volhard, C. The origin of pattern and polarity in the *Drosophila* embryo. *Cell* **68**, 201–219 (1992).
54. Ho, K., Dunin-Borkowski, O. M. & Akam, M. Cellularization in locust embryos occurs before blastoderm formation. *Development* **124**, 2761–2768 (1997).
55. Roonwal, M. L. Studies on the Embryology of the African Migratory Locust, *Locusta migratoria migratorioides* R. and F. I. The Early Development, with a New Theory of Multi-Phased Gastrulation among Insects. *Philos. Trans. R. Soc.* **226**, 391–421 (1936).
56. Dawes, R., Dawson, I., Falciani, F., Tear, G. & Akam, M. Dax, a locust Hox gene related to fushi tarazu but showing no pair-rule expression. *Development* **120**, 1561–1572 (1994).
57. Chodagam, S., Royou, A., Whitfield, W., Karess, R. & Raff, J. The centrosomal protein CP190 regulates myosin function during early *Drosophila* development. *Curr. Biol.* **15**, 1308–1313 (2005).
58. Ji, J.-Y., Haghnia, M., Trusty, C., Goldstein, L. S. B. & Schubiger, G. A genetic screen for suppressors and enhancers of the *Drosophila* cdk1-cyclin B identifies maternal factors that regulate microtubule and microfilament stability. *Genetics* **162**, 1179–1195 (2002).
59. Edgar, B. A., Kiehle, C. P. & Schubiger, G. Cell cycle control by the nucleocytoplasmic ratio in early *Drosophila* development. *Cell* **44**, 365–372 (1986).
60. Huang, J. & Raff, J. W. The disappearance of cyclin B at the end of mitosis is regulated spatially in *Drosophila* cells. *EMBO J.* **18**, 2184–2195 (1999).
61. Sarashina, I. et al. Location of micropyles and early embryonic development of the two-spotted cricket *Gryllus bimaculatus* (Insecta, Orthoptera). *Dev. Growth Amp Differ.* **47**, 99–108 (2005).
62. Ewen-Campen, B., Donoughe, S., Clarke, D. N. & Extavour, C. G. Germ cell specification requires zygotic mechanisms rather than germ plasm in a basally branching insect. *Curr. Biol.* **23**, 835–842 (2013).
63. Pechmann, M. et al. Striking parallels between dorsoventral patterning in *Drosophila* and *Gryllus* reveal a complex evolutionary history behind a model gene regulatory network. *eLife* **10**, e68287 (2021).
64. Church, S. H. et al. Insect egg size and shape evolve with ecology but not developmental rate. *Nature* **571**, 58–62 (2019).
65. Church, S. H. et al. A dataset of egg size and shape from more than 6700 insect species. *Sci. Data* **6**, 1–11 (2019).
66. Cadot, B., Gache, V. & Gomes, E. R. Moving and positioning the nucleus in skeletal muscle – one step at a time. *Nucleus* **6**, 373–381 (2015).
67. Bone, C. R. & Starr, D. A. Nuclear migration events throughout development. *J. Cell Sci.* **129**, 1951–1961 (2016).
68. Xiang, X. Nuclear movement in fungi. *Semin. Cell Dev. Biol.* **82**, 3–16 (2018).
69. Kokkoris, V., Stefani, F., Dalpé, Y., Dettman, J. & Corradi, N. Nuclear dynamics in the arbuscular mycorrhizal fungi. *Trends Plant Sci.* **25**, 765–778 (2020).
70. Kokkoris, V. et al. Host identity influences nuclear dynamics in arbuscular mycorrhizal fungi. *Curr. Biol.* **31**, 1531–1538.e6 (2021).
71. Potter, C. J., Tasic, B., Russler, E. V., Liang, L. & Luo, L. The Q system: a repressible binary system for transgene expression, lineage tracing, and mosaic analysis. *Cell* **141**, 536–548 (2010).
72. Donoughe, S., Kim, C. & Extavour, C. G. High-throughput live-imaging of embryos in microwell arrays using a modular specimen mounting system. *Biol. Open* **7**, bio.031260 (2018).
73. Preibisch, S. et al. Efficient Bayesian-based multiview deconvolution. *Nat. Methods* **11**, 645–648 (2014).
74. Preibisch, S., Saalfeld, S., Schindelin, J. & Tomancak, P. Software for bead-based registration of selective plane illumination microscopy data. *Nat. Methods* **7**, 418–419 (2010).
75. Schindelin, J. et al. Fiji: an open-source platform for biological-image analysis. *Nat. Methods* **9**, 676–682 (2012).
76. Hoffmann, J. & Donoughe, S. *hoffmannjordan/gryllus_nuclear_movements*: (Zenodo, 2022). <https://doi.org/10.5281/zenodo.6564745>.

Acknowledgements

This work was supported by funds from the National Science Foundation (NSF award IOS-1257217) and the Howard Hughes Medical Institute to CGE, a US Department of Energy (DOE) Computational Science Graduate Fellowship JH, a National Science Foundation Graduate Training Fellowship to S.D., and the Applied Mathematics Program of the US DOE Office of Advanced Scientific Computing Research under Contract DE-AC02-05CH11231 to CHR. TN was supported by a JSPS Overseas Research Fellowship (Received Number 693) from the Japan Society for the Promotion of Science. We thank the Extavour and Rycroft lab members, the Harvard Center for Biological Imaging, the NSF-Simons Center for Mathematical and Statistical Analysis of Biology at Harvard University, supported by NSF Grant DMS-1764269, and the Harvard Faculty of Arts and Sciences Quantitative Biology Initiative for discussion and support. We thank Julie Theriot for discussion of modeling approaches for nuclear movements and Rakeyah Ahsan for assistance with animal culture.

Author contributions

S.D. and C.G.E. conceived of the project; S.D. and T.N. performed all transgenic and imaging experiments; S.D. and J.H. analyzed the data; J.H. and C.H.R. designed and implemented all mathematical models in consultation with S.D., T.N. and C.G.E.; all authors contributed to writing of the manuscript.

Competing interests

The authors declare no competing interests.

Additional information

Supplementary information The online version contains supplementary material available at <https://doi.org/10.1038/s41467-022-31212-8>.

Correspondence and requests for materials should be addressed to Seth Donoughe, Chris H. Rycroft or Cassandra G. Extavour.

Peer review information *Nature Communications* thanks Ivo Telley and the other, anonymous, reviewer(s) for their contribution to the peer review of this work. Peer reviewer reports are available.

Reprints and permission information is available at <http://www.nature.com/reprints>

Publisher's note Springer Nature remains neutral with regard to jurisdictional claims in published maps and institutional affiliations.



Open Access This article is licensed under a Creative Commons Attribution 4.0 International License, which permits use, sharing, adaptation, distribution and reproduction in any medium or format, as long as you give appropriate credit to the original author(s) and the source, provide a link to the Creative Commons license, and indicate if changes were made. The images or other third party material in this article are included in the article's Creative Commons license, unless indicated otherwise in a credit line to the material. If material is not included in the article's Creative Commons license and your intended use is not permitted by statutory regulation or exceeds the permitted use, you will need to obtain permission directly from the copyright holder. To view a copy of this license, visit <http://creativecommons.org/licenses/by/4.0/>.

© The Author(s) 2022

Nuclear speed and cycle length co-vary with local density during syncytial blastoderm formation in a cricket

Supplemental Information

Seth Donoughe^{1,2,*}, Jordan Hoffmann³, Taro Nakamura^{1,4}, Chris H. Rycroft^{3,5,*}, Cassandra G. Extavour^{1,6,7,*}

Supplementary Notes

1	Processing, segmenting, and tracking microscopy datasets	2
1.1	Datasets from lightsheet microscopy	2
1.2	Datasets from epifluorescence microscopy	2
1.3	Datasets from confocal microscopy	3
1.4	Uses of each type of microscopy data	3
1.5	Accuracy of automated nucleus tracking	3
2	Quantitative measurements of nucleus behavior	4
2.1	Nucleus speed	4
2.2	Correlation of nucleus movement vectors	4
2.3	Local nucleus density	5
2.4	Rate of change in number of nuclei	5
2.5	Motion toward open space	6
3	Supplemental movie of yolk and nucleus movements	6
4	Simulating blastoderm formation with a pulling model	7
4.1	Model components	7
4.1.1	Embryo	7
4.1.2	Division geometry	7
4.1.3	Density-dependent cell cycle duration	8
4.1.4	Asymmetric pulling cloud	8
4.1.5	Bias of nucleus movement toward periplasm	9
5	Simulating blastoderm formation with pushing models	10
5.1	Symmetric mutual pushing	10
5.2	Asymmetric pushing by local clouds	10
6	Method for physically constricting embryos	12
6.1	Assembling the embryo constriction device	12
6.2	Using the embryo constriction device	12

* Corresponding authors. E-mail: donoughe@uchicago.edu, chr@seas.harvard.edu, extavour@oeb.harvard.edu

¹Department of Organismic and Evolutionary Biology, Harvard University, Cambridge, MA, USA

²*Present address:* Department of Molecular Genetics and Cell Biology, University of Chicago, Chicago, IL, USA

³John A. Paulson School of Engineering and Applied Sciences, Harvard University, Cambridge, MA, USA

⁴*Present address:* Division of Evolutionary Development, National Institute for Basic Biology, Okazaki, Japan

⁵Computational Research Division, Lawrence Berkeley Laboratory, Berkeley, CA, USA

⁶Department of Molecular and Cellular Biology, Harvard University, Cambridge, MA, USA

⁷Howard Hughes Medical Institute, Chevy Chase, MD, USA

References

15

Supplementary Note 1 Processing, segmenting, and tracking microscopy datasets

The *Methods* section of the main text includes information on animal culture, collecting embryos, mounting samples, and microscope settings. This section contains details on how we processed datasets for analysis.

Supplementary Note 1.1 Datasets from lightsheet microscopy

We fused multiview lightsheet datasets with the Multiview Reconstruction plugin^{1,2} for Fiji^{3,4} (version 2.0.0-rc-30 through 2.1.0/1.5.3). Fluorescent beads (ThermoFisher F8821) embedded in the agarose served as fiducial markers for registration; we used them to align and combine multiple views as a weighted average fusion¹. We deconvolved datasets for ten iterations with the Multiview Reconstruction plugin² on a 32-core workstation with 128 GB of RAM running Ubuntu 14.04.

We performed nucleus segmentation and automated tracking with Ilastik⁵ (versions 1.1.5 to 1.3.0). We imported all data as a 4D sequence, manually trained a pixel classifier to differentiate nuclei from background, and identified nuclei using the object classification tool. Then we used Ilastik's automated tracking tool to track all nucleus movements. We used a custom Mathematica script to convert the automated tracking output from Ilastik into an XML file that was parsable by MaMuT⁶, the semi-automated tracking plug-in for Fiji³. The script to generate the XML file, as well as those needed run the simulations in this study, are available on the GitHub repository that accompanies this paper (https://github.com/hoffmannjordan/gryllus_nuclear_movements). Note: the ability to directly transfer object tracks from Ilastik to MaMuT is now included in Ilastik (version 1.3.3). Last, we used MaMuT to manually identify each division and stitch together the Ilastik-generated tracks, which resulted in continuously tracked lineages. For embryos mounted in this manner, approximately two-thirds of the radial depth of the embryo could be imaged clearly (as measured from the surface to a center line connecting the anterior and posterior poles of the embryo), while the signal from the inner-most portion of the embryo was diffused by the yolk of the embryo.

Supplementary Note 1.2 Datasets from epifluorescence microscopy

We recorded multiple embryos at a time by tiling across a field of microwells, each of which held a single embryo, oriented laterally, following previously described methods⁷. We used Ilastik to segment and track nucleus movements and then manually identified divisions with MaMuT. For embryos mounted in this manner, approximately one-half to one-third of the *z*-depth of the embryo could be imaged clearly, while the signal from the rest of the embryo was diffused by the yolk of the embryo. Thus, the number of well-segmented nuclei fluctuated slightly between timepoints, depending on the particular paths traveled by individual nuclei; the effect of this variability was strongest for the first few division cycles. Therefore, for two-dimensional timelapse (2D+T) datasets, we performed automated analysis on these datasets beginning at the earliest timepoint when there were at least 50 visible nuclei.

Supplementary Note 1.3 Datasets from confocal microscopy

We recorded three-dimensional timelapse (3D+T) datasets of embryos laid by females with Act-mtdT and Act-H2B-EGFP transgenes⁸. We used a magnification such that approximately one-fifth of the length and one-half of the breadth of an embryo was recorded at a time. We cropped and assembled these into figures using Fiji. Details of the genotypes of these transgenic lines are included in the main text Methods section *Transgenesis and animal culture*.

Supplementary Note 1.4 Uses of each type of microscopy data

Multiview lightsheet datasets of blastoderm formation: These 3D+T datasets enabled us to reconstruct nucleus movements and divisions in detail. We recorded these datasets one at a time. After a syncytial blastoderm had formed, we removed the embryo from its agarose column and cultured it in an incubator as described in the main text Methods section *Collecting and culturing embryos*. Once the embryo hatched, we continued with processing and tracking the nuclei. We tracked and processed four such 3D+T datasets. Figures 1B, 1D, 2A-E, and 3A-H in the main text show data from a single such embryo (the same embryo in all cases). We followed the same procedures and repeated the same analyses on three additional lightsheet datasets. In all cases we found the same patterns shown in Figures 1, 2, and 3: a positive association between cycle duration and nuclear density, biphasic speeds within each cell cycle, a negative association between speed and density in Phase A, and a tendency for Phase A nuclei to move into nearby open space when they are in the interior of the embryo.

Epifluorescence datasets of blastoderm formation: We included three of these datasets in Fig. 5 in the main text as unmanipulated controls to compare to the physically constricted embryos.

Epifluorescence datasets of constricted embryos: We recorded 2D+T datasets of physically constricted embryos, imaged using epifluorescence. These data are shown in Fig. 5 of the main text. In our hands, constricted embryos did not hatch, and instead they arrested partway through development (in some cases before a blastoderm had formed, and in others afterwards). The furthest extent of development we observed was just before karyokinesis occurred⁹. Our criteria for including a constriction dataset in the data analysis were as follows: no visible ruptures of the eggshell, no cessation of nucleus movements before the syncytial blastoderm was formed, and no nuclear aggregations during the developmental period under study. In our recordings of unmanipulated embryos, we found that these criteria reliably predicted that blastoderm formation and subsequent development would proceed. We analyzed three constricted embryos that satisfied the criteria for inclusion (see Fig. 5 of the main text).

Confocal datasets of yolk and nucleus movement: We used these datasets to qualitatively assess the movements of yolk and nuclei. The results are shown in Fig. 1 of the main text and in Supplementary Movie 1.

Supplementary Note 1.5 Accuracy of automated nucleus tracking

To assess the accuracy of automated nucleus tracking for lightsheet datasets, we manually tracked a set of nuclei from an embryo and compared the nucleus positions to the output from automated tracking on the same dataset. Specifically, we took the first 300 successive frames and applied the semi-automated tracking tool in MaMuT⁶. Next, we inspected each nucleus position and tracking link and then manually corrected any incorrect positions or

links, resulting in 41,092 single-timepoint nucleus observations. Then, we used Ilastik to segment and automatically track the same dataset.

Treating the manually-corrected dataset as ground truth, we assessed the accuracy of the automated approach by calculating the distance from each nucleus in the manually-corrected dataset to the closest corresponding nucleus in the automatically-tracked dataset. Table 1 shows percentiles of these distances.

<i>Percentile</i>	<i>Distance (μm)</i>
10%	0.6
25%	0.9
50%	1.4
75%	1.9
90%	2.9

Table 1: **Tracking discrepancy.** Percentiles of spatial discrepancies between each nucleus in a manually tracked dataset and the closest corresponding nucleus in an automatically tracked dataset. We calculated distances for 41,092 manually tracked nucleus-timepoints.

Supplementary Note 2 Quantitative measurements of nucleus behavior

Supplementary Note 2.1 Nucleus speed

For 3D+T datasets, we defined a vector

$$\vec{x}_t = (x_t, y_t, z_t) \quad (1)$$

for a nucleus position at time t . Using this notation, we defined instantaneous nucleus speed, s_t , as half of the displacement per two timepoints,

$$s_t = \frac{1}{2} \|\vec{x}_{t+2} - \vec{x}_t\|, \quad (2)$$

which we converted to units of μm per minute. For 2D+T datasets, we defined speed in an analogous manner, calculating movement only in the xy plane. The z -component of motion was not available in such datasets, which meant that calculated speeds are an underestimate of the true nucleus speed in 3D space.

Supplementary Note 2.2 Correlation of nucleus movement vectors

For each embryo, we re-oriented the set of \vec{x}_t across all t so that the first principal component lay along the x axis, in effect rotating the dataset so that the long axis of the embryo was parallel to the x axis. By convention, we also oriented each embryo with the posterior end pointed toward the positive x direction. For each \vec{x}_t , we computed the motion vector from \vec{x}_t to \vec{x}_{t+2} , and then used it to calculate the correlation between pairs of nuclei moving at the same time (results shown in Fig. 1D of the main text).

Supplementary Note 2.3 Local nucleus density

We defined local nucleus density around a given focal nucleus as the number of other nuclei within radius $\mathcal{R} = 150 \mu\text{m}$.¹ For a nucleus near the periplasm of the embryo, the sphere of space within \mathcal{R} included some volume that was outside of the embryo itself, but we did not wish to include this space when calculating local nucleus density. Therefore, we needed to numerically represent the surface of the eggshell so that we could exclude the volume external to the embryo from consideration in calculating local density. We took a single timepoint at the uniform blastoderm stage that was imaged with a multiview lightsheet microscope, segmented the nuclei, and fitted a parabola to the anterior-posterior (A-P) axis of the cloud of points. We used this parabola to transform the positions of nuclei by mapping the parabola to a straight line. Then we calculated the convex hull of the transformed points, and applied the reverse transformation to the convex hull. This produced the volume \mathcal{B} .

We took the sphere \mathcal{S} defined by \mathcal{R} , and then defined

$$V = \text{volume}(\mathcal{S} \cap \mathcal{B}). \quad (3)$$

The volume fraction was computed as

$$\phi = \frac{V}{\frac{4}{3}\pi\mathcal{R}^3} \quad (4)$$

and the local density was defined as

$$\rho = \frac{\#}{\phi}, \quad (5)$$

where $\#$ represents the count of nuclei within \mathcal{R} .

For 2D+T datasets, local nucleus density was treated in an analogous manner: we computed the region of overlap of a $150 \mu\text{m}$ circle with the 2D convex hull of all nuclei at the blastoderm stage. Then we counted the number of nuclei within that area and calculated the area-weighted density as above. This meant that nuclear densities were calculated from volumes with different shapes in the 3D+T vs. 2D+T datasets (i.e. spherical vs. cylindrical), and therefore their measured values cannot be compared to one another in absolute terms. Instead, we consider it appropriate to compare density-dependent results between datasets that were imaged in the same manner.

Supplementary Note 2.4 Rate of change in number of nuclei

Early in cricket embryogenesis, we could not rule out the possibility that some nuclei passed through the middle of the embryo (see Supplementary Note 1.1), where their observable fluorescence signal was sufficiently diffuse that we could not detect and track the nuclei at all. Therefore, rather than counting nuclei directly at each timepoint, we used *percent change in nucleus number* as a proxy for nucleus division. Because the number of detected nuclei

¹We found that when we defined *local nucleus density* as the the number of other nuclei within $\mathcal{R} = 150 \mu\text{m}$, across the range of densities found during cricket blastoderm formation, we observed a positive association between local nucleus density and mitotic cycle duration (main text Fig. 2C-E). Similarly, we observed a negative association between local nucleus density and nucleus speed (main text Fig. 3E). We found that these results were not sensitive to the exact \mathcal{R} we that chose.

fluctuated slightly from one timepoint to the next, we smoothed the total number of nuclei present by applying a Gaussian blur with a width of three timepoints. Using Mathematica, an interpolant— $N(t)$ —was fitted through the data. We differentiated this function to produce $N'(t)$. To estimate a rate of change in the number of nuclei over time, we divided $N'(t)/N(t)$. As a result, percent change was briefly calculated to be negative in the first few division cycles.

Supplementary Note 2.5 Motion toward open space

We defined the direction “towards the largest open space” as the vector oriented towards the centroid of the 3D Voronoi cell formed by each nucleus, bounded by the inner surface of the eggshell, as approximated by the convex hull of nuclei at the blastoderm stage.

For each nucleus, we considered $\vec{v} = \frac{1}{2} (\vec{x}_{t+2} - \vec{x}_t)$, and calculated its correlation c with a vector into the direction into open space, \vec{s} , as

$$c = \frac{\vec{x} \cdot \vec{s}}{\|\vec{x}\| \|\vec{s}\|}. \quad (6)$$

To account for timepoint-to-timepoint noise in this calculation, we calculated average “movement into space” vectors for each nucleus over a sliding window of three timepoints. In addition, we computed the shortest distance from all nucleus locations \vec{x}_t to the inner surface of the eggshell, d_S . We binned nuclei by d_S into those that were near the surface ($d_S < 75 \mu\text{m}$) and those that were far from the surface ($d_S \geq 75 \mu\text{m}$), as shown in main text Fig. 3G,H.

Supplementary Note 3 Supplemental movie of yolk and nucleus movements

We have included an example movie as Supplementary Movie 1. This dataset was captured as follows:

- *Genotype*: Act-H2B-EGFP; Act-mtdT
- *Subject*: The field of view was centered 20% of the way from the anterior pole of the embryo, captured during the period of syncytial development when nuclei were initially reaching the anterior pole of the embryo.
- *Z-step*: $2.5 \mu\text{m}$
- *Duration*: 132 time-steps
- *Time interval*: 2 minutes
- *X – Y resolution*: 1 pixel = $0.327 \mu\text{m}$
- *Image processing*: 17 consecutive z -slices were combined as a maximal intensity projection (MIP). In order to image a given nucleus and its surrounding yolk, we only needed two to three z -slices of this thickness. We used more z -slices to capture more nuclei in a single video.

This movie illustrates that there are no obvious bulk flows of yolk, either during the phase when nuclei are moving (“Phase A”) or when they are relatively immobile (“Phase B”).

Supplementary Note 4 Simulating blastoderm formation with a pulling model

As described in the main text, the goal of our modeling approach was to assess whether a local, asymmetric, active pulling force on each nucleus could satisfactorily recapitulate the empirical patterns of nucleus behaviors. Here we report on the model in closer detail. The simulation is performed in a $202 \times 92 \times 92$ unit volume. We verified that results are consistent with scaling up the grid by a factor of two, but for time efficiency we opted to use the smaller grid. The simulation time step is $T = 45$ seconds, corresponding to half of a time-step from the lightsheet data. The embryo used for the fit of the simulation boundary was $2421 \mu\text{m}$ long, and thus the grid spacing is $L = 11.98 \mu\text{m}$.

Supplementary Note 4.1 Model components

We simulated the center of each nucleus $\vec{x}_i(t)$ as a function of time. The nucleus positions followed the differential equation

$$\alpha M \frac{d^2 \vec{x}_i}{dt^2} + \gamma \left(\frac{d\vec{x}_i}{dt} - \vec{v}^{cyt}(\vec{x}_i(t)) \right) = \vec{F}_i^{tot} \quad (7)$$

where M is an arbitrary mass scale and αM is the mass of a nucleus, γ is a drag coefficient between the nucleus and the cytoplasm, and \vec{F}_i^{tot} is the sum total of forces on the nucleus. Based on our experimental results, we assumed that $\vec{v}^{cyt} = \vec{0}$ and we did not simulate any viscous or viscoelastic flow in the cytoplasm. We worked in the overdamped limit where the acceleration could be neglected, yielding

$$\frac{d\vec{x}_i}{dt} = \frac{1}{\gamma} \vec{F}_i^{tot}. \quad (8)$$

We simulated equation (8) using the first-order forward Euler method. We describe the different contributions to the force below. We take $\gamma = 1M/T = 0.022M \text{ s}^{-1}$.

Supplementary Note 4.1.1 Embryo

We used the shape of a real cricket embryo, determined from the positions of nuclei during the uniform blastoderm stage, as described in Supplementary Note 2.3. We approximated each cross-section along the A-P axis z with an ellipse with radii $r_1(z)$ and $r_2(z)$ with a center at $(x(z), y(z))$. This defined a boundary \mathcal{B} . For simulated *G. bimaculatus* embryos, we performed all calculations on the discretized 3D grid.

The grid was used by the scikit-fmm library, which we used to compute the clouds for each nucleus.

Supplementary Note 4.1.2 Division geometry

Nuclei divided in random directions (i.e. with random spindle orientation) throughout the simulation, irrespective of the proximity of neighbors, the proximity of the eggshell, or the orientation of previous divisions in a lineage. Newly divided daughter nuclei were created at $\vec{x}^{mother} \pm \vec{n}(1 \mu\text{m})$, where \vec{n} is a random unit normal. If this displacement resulted in a daughter nucleus landing outside the boundary of the embryo, we assigned a new position for the nucleus by projecting it back to the surface of the embryo boundary by finding the closest point on the surface.

Supplementary Note 4.1.3 Density-dependent cell cycle duration

In the empirical data, we observed a strong positive association between local nucleus density and cell cycle duration (see Fig. 2 in the main text). We incorporated this relationship into our simulation directly. We fitted a logistic curve to the empirical density vs. cell cycle duration data (shown in Fig. 2 in the main text), and then drew from it with normally distributed noise, based on the density at nucleus birth. In the real embryos, we observed that the variation in cycle duration increased as density increased (Fig. 2C-E), so we fitted the variance to a global clock used in the simulation, $(90 \text{ s}) + (270 \text{ s})(t - T)/T$, where T was the total simulation time.

Supplementary Note 4.1.4 Asymmetric pulling cloud

We hypothesized that there was a local, asymmetric, active pulling force on each nucleus. We describe the biological inspiration for this model in the main text. Here we describe the implementation of the model.

Our force calculation models the nuclei as spheres with a $7.2 \mu\text{m}$ diameter. We modeled the motion of a nucleus by ascribing a pulling cloud that emerges from a single origin on the surface of the nucleus. The cloud grows uniformly in all directions to a maximal radius, $R_{\text{max}} = 150 \mu\text{m}$, except for where its growth is impeded by the surface of the nucleus from which it originated, the surface of another cloud region, or the inner surface of the eggshell. In the simulated embryo, during the earliest portion of development, some of the nuclei—namely those that are on the expanding “front”—have clouds that reach the maximum radius. Later on, however, virtually all of the nuclear clouds become occluded by other clouds or by the eggshell boundary before they reach the maximum radius. This pattern of increasing density qualitatively matches the decrease in neighbor distances among nuclei in the empirical datasets. For instance, when there are ~ 100 nuclei, the neighbor distance is $132 \mu\text{m} \pm 33 \mu\text{m}$ (mean \pm standard deviation); at ~ 350 nuclei it is $78 \mu\text{m} \pm 35 \mu\text{m}$; at ~ 1200 nuclei it is $40 \mu\text{m} \pm 14 \mu\text{m}$.

For each nucleus, we computed this cloud region by using the Python library `scikit-fmm`¹⁰. We used the fast marching method¹¹, which is a computationally efficient way to identify all the voxels in the discretized grid that should be assigned to each nucleus. Specifically, we initialized the locations of nuclei to be zeroes of a field $T(\vec{x})$. We then solved the Eikonal equation

$$|\nabla T(\vec{x})| = 1, \quad (9)$$

where $T(\vec{x})$ describes the minimum travel time from a nucleus to each position. The fast marching method works by scanning outward from the nuclei positions to fill in the values of the $T(\vec{x})$ on the discretized grid. It also keeps

track of which nucleus is closest to each point \vec{x} . This allows us to efficiently compute the region \mathcal{R}_i that is closest to each nucleus \vec{x}_i . From here, we define the pulling cloud region \mathcal{V}_i by removing space that is further away than R_{\max} , and space that is occluded by the steric effects from the nucleus (*i.e.* where a ray from the cloud origin to \vec{x} intersects the nucleus).

Each point in the cloud region creates a tug toward its position. Since our model is inspired by pulling forces on astral microtubules, we scale the tug by a factor of $1/r^2$ to account for the microtubule density, where r is the distance to the nucleus center.² Hence, the total force created by the cloud is given by the integral

$$\vec{F}_i^{\text{cloud}} = \int_{\mathcal{V}_i} \beta \frac{\vec{y} - \vec{x}_i}{\|\vec{y} - \vec{x}_i\|_2^3} d\vec{y}. \quad (10)$$

The parameter $\beta = 0.00521M/T^2 = 2.57 \times 10^{-6} \text{ M s}^{-2}$ was fit from experimental data where we matched the maximum speed at the 4-nucleus stage. The integral in Eq. (10) is performed by summing over all voxels in \mathcal{V}_i .

Supplementary Note 4.1.5 Bias of nucleus movement toward periplasm

In *G. bimaculatus* embryos, the first zygotic division tends to occur about ~60% of the way along the A-P axis, as measured from the anterior pole of the embryo. During the first few cell cycles, nuclei spread apart in space, with some of them moving through “open space” across the yolk-rich middle of the embryo, and others moving within the periplasm, close to the inner surface of the eggshell. The nuclei ultimately move into the periplasm and stay there (see Fig. 1A, B). Because nuclei travel varied paths and arrive in the periplasm asynchronously, we model their eventual movement into the periplasm as a small bias that contributes additively to their movement. Specifically, for each nucleus \vec{x}_i we introduced a component to a nucleus’s motion vector that is in the direction of the nearest point \vec{y}_i on the inner surface of the eggshell. We define the vector $\vec{q}_i = \vec{y}_i - \vec{x}_i$. The contribution to the force is given by

$$\vec{F}_i^{\text{surface}} = \zeta \|\vec{F}_i^{\text{cloud}}\| \frac{\vec{q}_i}{\|\vec{q}_i\|} \quad (11)$$

where ζ is a dimensionless constant. We include a factor $\|\vec{F}_i^{\text{cloud}}\|$ since it is an existing force scale in the model. We used a value of $\zeta = \frac{1}{3}$ to match the bias towards the periplasm in the empirical data.

It is not known what causes the empirical tendency for nuclei to move towards the periplasm. One possibility is that there is a bias in the direction of active force generation associated with each nucleus. We do not currently have empirical evidence in favor of or against this hypothesis, but it will be an important topic for future work.

²Technically it would be more consistent with the model to normalize by $1/\tilde{r}^2$, where \tilde{r} is the distance to the cloud origin on the nucleus surface. However, this could create numerical difficulties since the cloud origin is on the boundary of \mathcal{V}_i and thus \tilde{r} can become arbitrarily small. Since the cloud origin and nucleus center are close, using r instead of \tilde{r} has a minimal effect on the outcome and is more numerically stable.

Supplementary Note 5 Simulating blastoderm formation with pushing models

An alternative to the “pulling” model described above in Supplementary Note 4 is one in which repulsive forces generate nuclear movements¹². We assessed two different “pushing” models, as described below.

Supplementary Note 5.1 Symmetric mutual pushing

We replaced our calculation of cloud-based pulling forces with the mutual repulsion forces presented by Dutta and colleagues¹³, which was tuned on a later stage of *Drosophila melanogaster* development. With this model, there is a decay in nuclear speed as nuclei separate from one another (see Equation 2¹³). This is the opposite of what we observe in real *G. bimaculatus* embryos (main text Fig. 3E) and in simulations that use pulling clouds (main text Fig. 4J). In both cases, nuclei that move fastest are those that are farthest from other nuclei (main text Fig. 3D, 4I). Therefore, we concluded that a mechanism based on symmetric mutual repulsion does not effectively explain nucleus movements in *G. bimaculatus*.

Supplementary Note 5.2 Asymmetric pushing by local clouds

In Supplementary Note 4 we presented a model in which a cloud around a nucleus exerts a pulling force on it. We also tested a model that was equivalent in all ways except that the clouds exert *pushing* forces instead (schematized in Fig. S1). We found that this asymmetric pushing model led to nuclear dynamics that were very different from the pulling model, and which were also incompatible with our empirical observations.

To implement the asymmetric pushing model, we modified the force of the cloud (originally given in Equation 10) to be

$$\vec{F}_i^{\text{cloud}} = \int_{\mathcal{V}_i} \beta \frac{\vec{x}_i - \vec{y}}{\|\vec{y} - \vec{x}_i\|_2^3} d\vec{y}, \quad (12)$$

where \vec{x}_i and \vec{y} have been swapped in the numerator. Again the parameter β was fit to match the maximum speed at the 4-nucleus stage. We kept the rest of the model as described in Supplementary Note 4. The most striking outcome of this model is that the simulated nuclei bunch together rather than spread apart. In its implementation, this required a finer simulation domain and a smaller time-step to ensure that nuclei would not be forced to pass through one another within a single time-step.

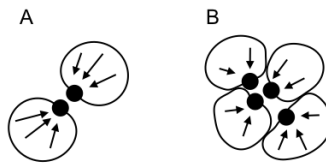


Figure S1: **Schematic of asymmetric pushing model.** **A**, After a division, two nuclei are relatively close to one another and their pushing clouds are opposed to each other. Pushing from the clouds will cause the two nuclei to move closer to one another. **B**, As the nuclei divide, a clump of nuclei will form.

If two nuclei are nearer to each other than they are to any other nuclei—as happens immediately after a division—their shells will continue pushing the two nuclei towards one another. This process continues, and as nuclei continue to divide, a clump of nuclei forms as shown in Fig. S2. The local density of each nucleus thus rapidly rises

and, due to the density-dependent division cycle, causes the cycle length of the nuclei to rapidly increase. Under this pushing model, the nuclei do not expand throughout the cytoplasm, as is seen in the empirical data. If local asymmetric pushing forces are in fact operating in the syncytial embryos of *G. bimaculatus*, we hypothesize that an additional mechanism is present to localize those pushing forces so that they occur primarily in the region *between* adjacent nuclei. Alternatively, repulsive forces could emerge as direct cloud-to-cloud interactions, possibly resulting from interdigitating MTs, as has been observed in *D. melanogaster*^{12,14}.

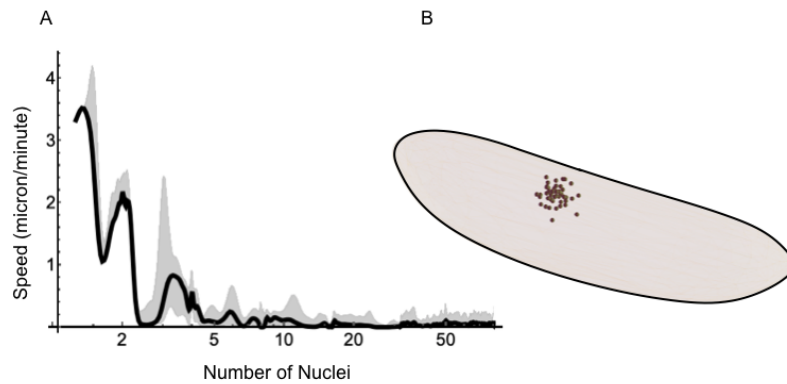


Figure S2: **Simulation results from the asymmetric pushing model.** **A**, Nuclear speeds as the total number of nuclei increases. **B**, A snapshot from the model at the 46-nucleus stage. Note that the nuclei are clumped together, unlike in the asymmetric pulling model simulation (main text Fig. 4G) or in the empirical data (main text Fig. 4F).

Supplementary Note 6 Method for physically constricting embryos

Supplementary Note 6.1 Assembling the embryo constriction device

We constricted embryos in a custom device, constructed as follows: We used a laser cutter to cut the components from sheets of acrylic (thickness = 1.59 mm, McMaster-Carr 8560K172; thickness = 3.18 mm, McMaster-Carr 8560K257), and then assembled them with acrylic welding solution (IPS Weld-On 3 Acrylic Plastic Cement) following the procedure described previously⁷. A DXF design file of the acrylic components is included with the present manuscript, labeled Supplementary Software 1. The device's construction also required a common binder clip (width = 20 mm), two steel nails (diameter = 2 mm; length = 39 mm), and a rubber band (thickness = 1 mm). We were able to successfully constrict embryos with versions of the device that were assembled with several different types of nails, rubber bands, and binder clips. We used a human hair as the constricting fiber. It was held in place by being pinched in a block of elastomer (Dow Corning Sylgard 184 Elastomer Kit) into which a slit had been cut with a razor blade. We used a crafting hot glue gun to attach acrylic components to non-acrylic components. Schematics of all components are shown to scale along with additional assembly instructions in Fig. S3.

Supplementary Note 6.2 Using the embryo constriction device

Figure S4A is a photograph of the device in use, with human hairs used as the constricting fibers. We placed embryos in water-filled acrylic troughs on a removable platform, and then constricted them one at a time. To do so, we threaded a hair through the removable plastic platform, around an embryo, back through a hole at the bottom of a trough in the removable platform, and then attached it to a ratchet mechanism. Detailed instructions for this procedure are shown in Fig. S4B. This allowed us to increase tension on the hair while observing the embryo under a dissection microscope. As we increased tension, the embryo was incrementally constricted. After the desired extent of constriction was achieved, we placed temporary dabs of hot glue to affix the hair in place for the duration of imaging.

The device was able to hold multiple constricted embryos at a time for simultaneous imaging, up to a maximum of seven embryos. Once a set of embryos was constricted, we took the removable platform from the constriction device, placed it in a glass bottom 6-well dish (MatTek Po6G-1.5-20-F), and imaged it using a Zeiss Cell Discoverer microscope following previously described methods⁷.

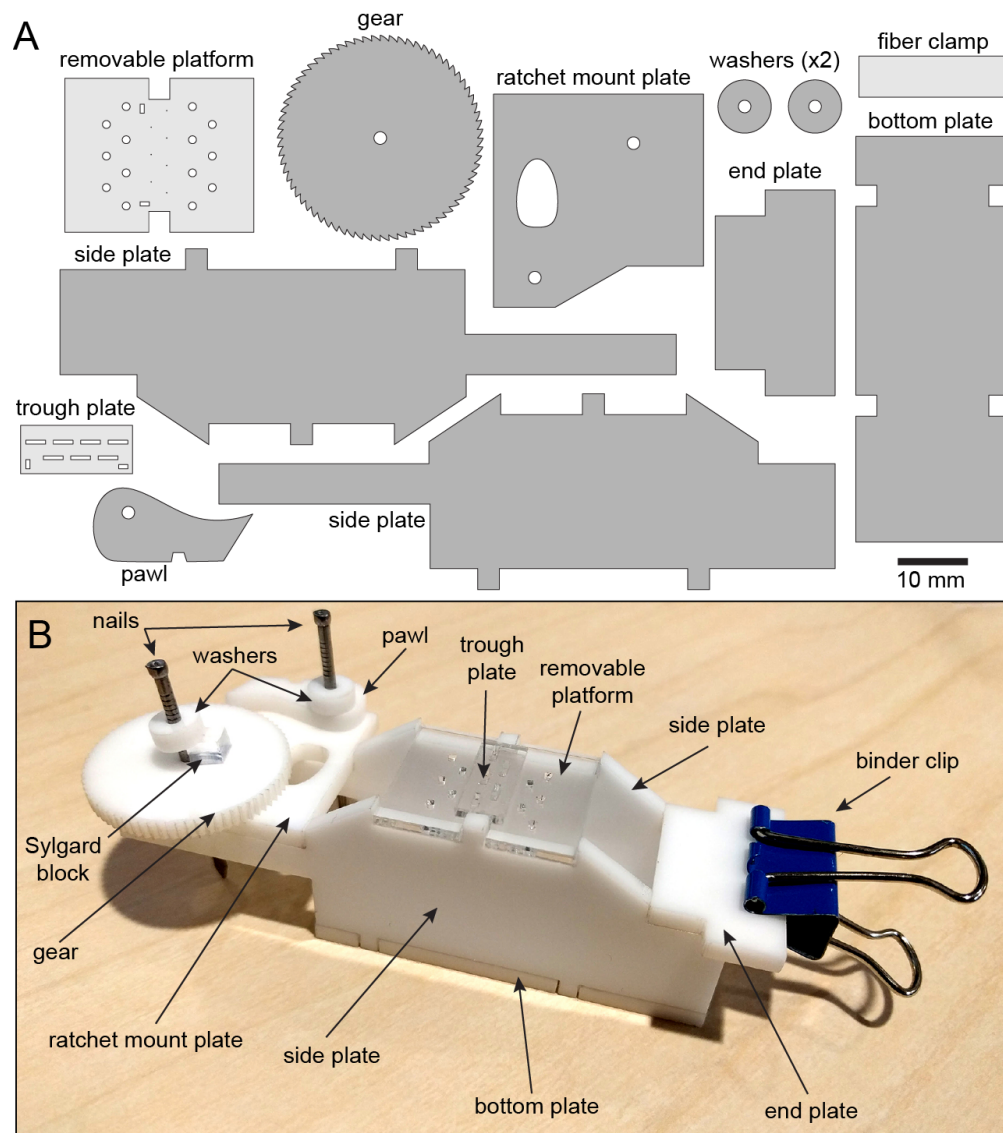


Figure S3: **Assembling a device for constricting embryos.** **A**, Diagram of all acrylic components. We cut the light gray pieces from 1.59 mm-thick acrylic sheet. We cut the rest from 3.18 mm-thick acrylic sheet. **B**, The assembled device also included a binder clip and two steel nails. Before welding the trough plate to the removable platform, we positioned trough plate so that the rectangular holes in the platform lined up with the corresponding holes in the trough plate. After the rest of the components were welded together as shown, we inserted one steel nail through a washer, then through the pawl, then through the ratchet mount plate. We applied hot glue to the top of the washer, fixing it to the nail. We also applied hot glue to the underside of the ratchet mount plate where the nail emerged, fixing the nail to the plate. We used a straight edge razor to cut a block of Sylgard elastomer with approximate dimensions 4 mm × 8 mm × 8 mm, and then sliced the block through half its depth when oriented with the largest face flat on a table. We inserted the second nail through the other washer, gear, and then the ratchet mount plate. We positioned the Sylgard block as shown, and then hot glued to the gear. We applied hot glue to the top of the second washer, fixing it to the nail. Finally, we applied more hot glue to the nail where it emerged underneath the ratchet mount plate, fixing it in place.

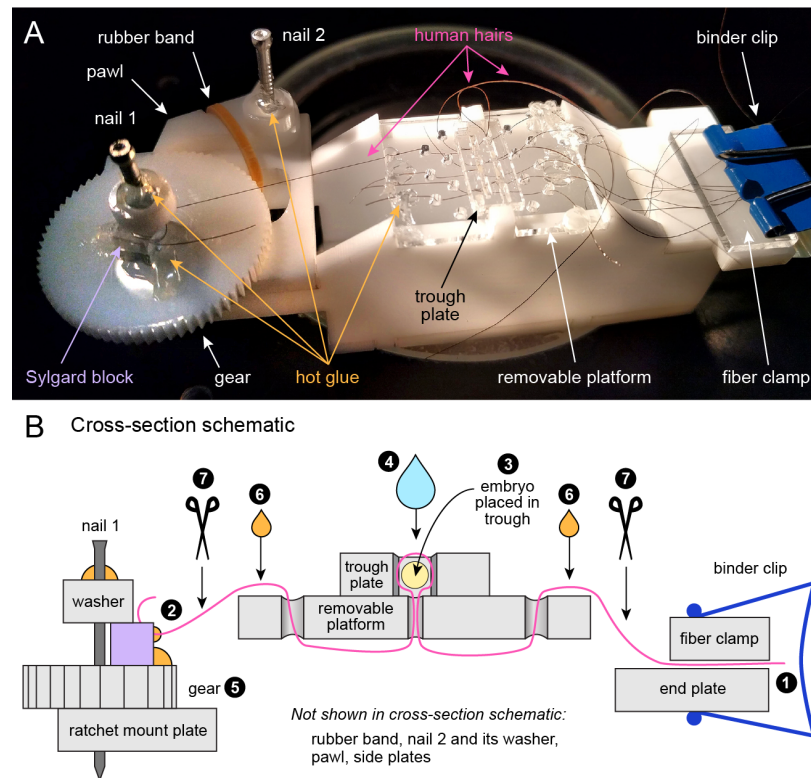


Figure S4: Constricting embryos. **A**, Photograph of the constriction device in use on a dissection microscope. To prepare the device for use, we cut a small rubber band to linearize it, inserted it through the largest hole in the ratchet mount plate, wrapped it underneath the side plate, and then rejoined it to itself by tying a knot. The re-joined rubber band formed a loop with the band slotting into the notch on the pawl, as shown. The tension on the rubber band pushed the pawl against the gear to make a ratchet. White arrows highlight the rubber band, binder clip, fiber clamp, removable platform, and gear. Hot glue is indicated with orange arrows. Note: the hot glue, rubber band, and fiber clamp were not depicted in Fig. S3. The fiber clamp was an unattached rectangle of acrylic that, when squeezed by the binder clip, effectively held the fibers clamped in place. **B**, Cut-away schematic of fiber threading path (not to scale). Acrylic components are depicted in light gray, nail in dark gray, Sylgard block in lavender, hot glue in orange, water in light blue, and binder clip in dark blue. The embryo is shown in yellow as a cross-section end-on. The constricting fiber (a human hair) is shown in pink. Procedure for constricting embryos:

1. We clamped one hair between the end plate and fiber clamp.
2. We threaded the hair by hand through the path shown, and ultimately inserted into it the slit in the elastomer block, leaving a large loop in the place around the trough where the embryo would go. The removable platform can be taken off of the device to make threading easier.
3. We placed the embryo into the trough.
4. We added distilled water to the trough to fill its entire volume.
5. We manually cranked the gear while the embryo was observed by the user with a dissection microscope. Surface tension kept the water from leaking through the bottom hole.
6. When the desired constriction was achieved, we used hot glue to affix the hair at the two locations indicated with orange droplets.
7. We used scissors to cut the hair at the two locations indicated with the scissors icons. We repeated the constriction process on multiple embryos and then removed the removable plate. To image the embryos, we inverted the removable plate, with constricted embryos still in the troughs, and placed it into a coverslip-bottomed dish. We filled the dish with distilled water, and then imaged the embryos with an inverted microscope.

References

1. Preibisch, S., Saalfeld, S., Schindelin, J. & Tomancak, P. Software for bead-based registration of selective plane illumination microscopy data. *Nature Methods* **7**, 418–419 (2010).
2. Preibisch, S. *et al.* Efficient Bayesian-based multiview deconvolution. *Nature Methods* **11**, 645–648 (2014).
3. Schindelin, J. *et al.* Fiji: an open-source platform for biological-image analysis. *Nature Methods* **9**, 676–682 (2012).
4. Schindelin, J., Rueden, C. T., Hiner, M. C. & Eliceiri, K. W. The ImageJ ecosystem: An open platform for biomedical image analysis. *Molecular Reproduction and Development* **82**, 518–529 (2015).
5. Berg, S. *et al.* ilastik: Interactive machine learning for (bio) image analysis. *Nature Methods* **16**, 1226–1232 (2019).
6. Wolff, C. *et al.* Multi-view light-sheet imaging and tracking with the MaMuT software reveals the cell lineage of a direct developing arthropod limb. *eLife* **7** (2018).
7. Donoughe, S., Kim, C. & Extavour, C. G. High-throughput live-imaging of embryos in microwell arrays using a modular specimen mounting system. *Biology Open* **7**, bio031260 (2018).
8. Nakamura, T. *et al.* Imaging of transgenic cricket embryos reveals cell movements consistent with a syncytial patterning mechanism. *Current Biology* **20**, 1641–1647 (2010).
9. Donoughe, S. & Extavour, C. G. Embryonic development of the cricket *Gryllus bimaculatus*. *Developmental Biology* **411**, 140–156 (2016).
10. The scikit-fmm Team. in (2019). <https://github.com/scikit-fmm/scikit-fmm> (2020).
11. Sethian, J. A. *Level set methods and fast marching methods* tech. rep. (Cambridge University Press, 1999).
12. Baker, J., Theurkauf, W. E. & Schubiger, G. Dynamic changes in microtubule configuration correlate with nuclear migration in the preblastoderm *Drosophila* embryo. *The Journal of Cell Biology* **122**, 113–121 (1993).
13. Dutta, S., Djabrayan, N. J.-V., Torquato, S., Shvartsman, S. Y. & Krajnc, M. Self-similar dynamics of nuclear packing in the early *Drosophila* embryo. *Biophysical Journal* **117**, 743–750 (2019).
14. Deshpande, O., de-Carvalho, J., Vieira, D. V. & Telley, I. A. Astral microtubule cross-linking safeguards uniform nuclear distribution in the *Drosophila* syncytium. *Journal of Cell Biology* **221**, e202007209 (2021).